1 **Timing landslide and flash flood events from SAR satellite: a regionally applicable**

2 **methodology illustrated in African cloud-covered tropical environments**

3 Axel A.J. Deijns[1,2,*], Olivier Dewitte[1], Wim Thiery[2], Nicolas d'Oreye[3,4], Jean-Philippe Malet[5], François

4 Kervyn[1]

5 [1] Department of Earth Sciences, Royal Museum for Central Africa, 3080 Tervuren, Belgium
6 [2] Department of Hydrology and Hydraulic Engineering, Earth System Science, Vrije Universiteit Brussel,
7 1050 Elsene, Belgium
8 [3] Department of Geophysics/Astrophysics, National Museum of Natural History, 7256 Walferdange,
9 Luxembourg
10 [4] European Center for Geodynamics and Seismology, 7256 Walferdange, Luxembourg
11 [5] École et Observatoire des Sciences de la Terre & Institut Terre et Environnement de Strasbourg, Centre
12 National de la Recherche Scientifique, University of Strasbourg, F-67000 Strasbourg Cedex, France
13 [*] Corresponding Author. Email: axel.deijns@africamuseum.be

14 **Abstract**

15 Landslides and flash floods are geomorphic hazards (GH) that often co-occur and interact. They

16 generally occur very quickly, leading to catastrophic socioeconomic impacts. Understanding the

17 temporal patterns of occurrence of GH events is essential for hazard assessment, early warning and

18 disaster risk reduction strategies. However, temporal information is often poorly constrained, especially

19 in frequently cloud-covered tropical regions, where optical-based satellite data is insufficient. Here we

20 present a regionally applicable methodology to accurately estimate GH event timing that requires no

21 prior knowledge of the GH event timing, using Synthetic Aperture Radar (SAR) remote sensing. SAR can

22 penetrate through clouds and therefore provides an ideal tool for constraining GH event timing. We use

23 the open-access Copernicus Sentinel-1 (S1) SAR satellite that provides global coverage, high spatial

24 resolution (~10-15 m) and a high repeat time (6-12 days) from 2016 to 2020. We investigate the

25 amplitude, detrended amplitude, spatial amplitude correlation, coherence and detrended coherence

26 time series in their suitability to constrain GH event timing. We apply the methodology on four recent

27 large GH events located in Uganda, Rwanda, Burundi and DRC containing a total of about 2500 manually

28 mapped landslides and flash flood features located in several contrasting landscape types. The

29 amplitude and detrended amplitude time series in our methodology do not prove to be effective in

30 accurate GH event timing estimation, with estimated timing accuracies ranging from a 13 day to a 1000

31 day difference. A clear increase in accuracy is obtained from SAC with estimated timing accuracies

32 ranging from a 1 day to an 85 day difference. However, the most accurate results are achieved with

33 coherence and detrended coherence with estimated timing accuracies ranging from a 1 day to a 47 day

34 difference. The amplitude time series reflect the influence of seasonal dynamics, which cause the timing

35 estimations to be further away from the actual GH event occurrence compared to the other data

36 products. Timing estimations are generally closer to the actual GH event occurrence for GH events

37 within homogenous densely vegetated landscape, and further for GH events within complex cultivated

38 heterogenous landscapes. We believe that the complexity of the different contrasting landscapes we

39 study is an added value for the transferability of the methodology and together with the open access

40 and global coverage of S1 data it has the potential to be widely applicable.

1. Introduction

Landslides and flash floods are geomorphic hazards (GH) that can occur very quickly, sometimes in a matter of a few hours. GH frequently co-occur and interact (e.g. Rengers et al., 2016), they have a significant impact on the landscape (Petersen, 2001, Korup et al., 2010) and are severe threats for infrastructure and human life (Bradshaw et al., 2007, Kjekstad and Highland, 2009, Froude and Petley, 2018). Landslides and flash floods are often studied in isolation. However, it is their combined occurrence that can lead to more extreme impacts. For example, in 2013, several people were killed and ~7000 lost their homes in the Rwenzori Mountains in Uganda by a single debris-rich flash flood fed by upstream landslides (Jacobs et al., 2016a). Also, in 2011, a combination of flash flooding and mudslides across the highlands of the state of Rio de Janeiro claimed the lives of 916 people and left 35.000 people homeless (Marengo & Alves, 2012).

Understanding the temporal occurrence of GH events is essential for hazard assessment, early warning, and disaster risk reduction strategies (van Westen et al., 2008, Ali et al., 2017, Liu et al., 2018, Guzzetti et al. 2020). Temporal information with a few day accuracy is needed to understand the close association between precipitation and the occurrence of GH events (Guzzetti et al., 2008; 2020, Turkington et al., 2014, Marc et al., 2018). For site-specific and local-scale investigation, this accurate information on the timing of GH events can be obtained with field-based approaches such as watershed/hillslope monitoring (Guzzetti et al., 2012) or a network of observers (Jacobs et al., 2019, Sekajugo et al., 2022). However, when information on the timing of GH events is needed at a regional level, the acquisition of such data can only be achieved with satellite remote sensing (Joyce et al., 2009, Le Cozannet et al., 2020), especially in mountainous regions with difficult field accessibility and where monitoring and observation capacities are limited (Dewitte et al., 2021).

Satellite remote sensing, and more specifically the use of optical imagery, is a well-developed field of research to accurately determine the location of GH (Stumpf et al., 2014, Behling et al., 2014; 2016, Mohan et al., 2021). Optical-based satellite approaches can also be used for extracting the information on the timing of the GH events (e.g. Kennedy et al., 2018, Deijns et al., 2020), however such approaches are of limited use in cloud-covered environments, especially if temporal information with a few day accuracy is needed.

Synthetic Aperture Radar (SAR) satellite, being an active system with an ability to penetrate cloud cover, holds a great potential for characterizing the timing of GH. Additionally, the sensitivity of SAR satellite data to surface changes, including vegetation changes (Hagberg et al., 1995, Balzter, 2001, Barrett et al., 2012), soil moisture changes (Dobson & Ulaby, 1986, Dubois et al., 1995, Ulaby et al., 1996, Nolan & Fatland, 2003, Srivastava et al., 2006), and surface texture changes (Dzurisin, 2006) gives SAR the potential to display GH timing with an accuracy of days.

SAR derived products typically used for GH (event) analysis are amplitude data (i.e. changes in surface backscattering intensity of SAR signal between two images) (e.g. Mondini et al., 2017; 2019, Esposito

77 et al., 2020, DeVries et al., 2020, Handwerger et al., 2022) for which amplitude correlation is a common
78 method used in amplitude change detection (Mondini et al., 2017, Konishi & Suga, 2018, Jung and Yun,
79 2020) and the coherence (i.e. the change in the ability of SAR wave fronts to stay spatially and/or
80 temporally in phase between the two images of an interferometric pair) (Burrows et al., 2019; 2020,
81 Tzouvaras et al., 2020). Additionally, there is a wide range of studies that use SAR-derived ground
82 deformation to map landslides (Casagli et al., 2017, Solari et al., 2020) or analyze pre-cursor movements
83 (Intrieri et al., 2018) and internal variability (Nobile et al., 2018). However, they are dependent on
84 consistent high coherence values at the GH locations, which will make these methods of limited use in
85 highly vegetated landscapes (e.g. the tropics) (Komac et al., 2015, Solari et al., 2020) and for fast
86 moving GH (e.g. shallow landslides and flash floods) (Burrows et al., 2020; Tzouvaras et al., 2020). In
87 recent GH detection studies, amplitude products are usually preferred over coherence products (Ge et
88 al., 2019, Jung and Yun, 2020, Mondini et al., 2021), since coherence generally yields less accurate
89 results due to lower resolution (Burrows et al., 2019; 2020) and a higher number of false-positives
90 (Aimaiti et al., 2019, Jung and Yun, 2020). Despite the increasing use of SAR imagery for GH detection
91 (Martinis et al., 2015, Psomiadis, 2016, Twele et al., 2016, Mondini et al., 2019, Burrows et al., 2020,
92 Jung and Yun, 2020, Tzouvaras et al., 2020, Jacquemart and Tiampo, 2021, Handwerger et al., 2022),
93 to date, only the recent study of Burrows et al. (2022) used SAR to refine the timing of GH inventories.
94 Although located in the tropics and showing accurate results, their study was only applied (1) within a
95 relatively densely vegetated landscape, (2) only on landslides, (3) using pre-processed amplitude
96 imagery with Google Earth Engine (GEE) (Gorelick et al., 2017), (4) with a-priori knowledge on the
97 timing of the event (i.e. the year). GH events occur within a variety of landscapes (Emberson et al.,
98 2020, Dewitte et al., 2021). Therefore, there is a clear need to calibrate and validate any GH timing
99 method for varying landscape, and land use/land cover characteristics. Additionally, the frequent co-
100 occurrence of landslides and flash floods (Jacobs et al., 2016b, Rengers et al., 2016) warrants the need
101 to analyze them using a combined methodology. However, so far, there has never been research
102 dedicated to their combined temporal detection using radar satellite.

103 The Copernicus Sentinel-1 (S1) constellation is frequently used in GH detection studies (Mondini et al.,
104 2021). Next to the fact that it is freely available and acquired regionally (from 2016 onwards), it offers
105 a very good trade-off between frequency of acquisition (6/12 days) and spatial resolution (10-15 m
106 depending on the pre-processing parameters). These advantages make S1 an attractive tool to integrate
107 in a regional GH timing methodology.

108 In this study, we aim to develop a regionally applicable methodology that automatically estimates GH
109 event timing using S1 SAR imagery on GH events spatially located, but with unspecified timing. We
110 analyze landslides and flash floods together as being co-occurring and interacting events. We create a
111 methodology that can be applied at the regional scale in complex and various topographic and land
112 use/land cover environments. The methodology is developed using four GH events either containing
113 landslides, or a combination of landslides and flash floods located in contrasting landscape types
114 observed within tropical Africa (see section 2.1). We analyze an unprecedented amount of S1 SAR

products, namely: amplitude, spatial amplitude correlation (a metric based on the common amplitude correlation) and coherence. Specifically, we: (1) create S1 SAR time series and analyze their patterns and behavior at the location of several GH events, (2) demonstrate and assess the ability to detect the timing of GH events using changes within the S1 SAR time series and, (3) investigate the influences of the landscape characteristics on the ability to derive the timing from S1 SAR timeseries through a sensitivity analysis.

2. Data

2.1. Selection of GH events in a tropical region with diverse landscapes

We focus on the western branch of the East African Rift, a mountainous region with high population densities and diverse landscape and land use/land cover characteristics (Depicker et al., 2021, Dewitte et al., 2021). The region has a bimodal precipitation distribution with two rainy peaks (October-November & March-April) and a main dry season (June-August) associated with the North-South migration of the Inter Tropical Convergence Zone (ITCZ) (Thiery et al., 2015, Nicholson, 2017, Monsieurs et al., 2018a) with annual precipitation ranging from ~0.8m along the shores of Lake Tanganyika to easily more than 2m in the highlands, with the maximum in the Rwenzori Mountains (Monsieurs et al., 2020, Van de Walle et al., 2020). The seasonality of the precipitation strongly controls the occurrence of landslides and flash floods (Jacobs et al., 2016a; 2016b, Monsieurs et al., 2018a; 2018b, Kubwimana et al., 2021). Vegetation dynamics are high in the cultivated areas due to the variety of cropping practices (crop rotations and shifting cultivation, Heri-Kazi & Bielders, 2021). Moreover, the region is one of the most cloud-covered places in the world (Robinson et al., 2019) and a global hotspot of thunderstorm activity (Thiery et al., 2016; 2017, Peterson et al., 2021).

We investigate four GH events with known days of occurrence, and located in contrasting landscapes (fig. 1):

- Event 1 (Uganda GH event) is located in the southern part of the Rwenzori Mountains (Uganda) and counts 1063 landslide features of which some contribute directly to the sediment load of the valley river (fig. 1, Uganda). The event occurred between the 21st and the 22nd of May 2020. The terrain consists of pristine forests and some cultivated landscape (fig. 2a).
- Event 2 (Rwanda GH event) is located in the Karongi district (western Province, Rwanda) and counts 494 features composed of both landslide and flash floods and occurred on the 6th of May 2018 (fig. 1, Rwanda). The terrain consists of an inhabited and highly cultivated landscape with the presence of agricultural terraces (fig. 2b).
- Event 3 (Burundi GH event) occurred around the hills of Nyempundu in the Cibitoke region (north Burundi) and counts 318 features composed of landslides and flash floods and occurred between the 4th and 5th of December 2019. Here, many landslides contribute directly to the sediment load of the rivers (fig. 1, Burundi). The terrain consists of inhabited cultivated landscape and sporadic tree cover (fig. 2c).

- Event 4 (DRC GH event) occurred west of the city of Uvira (DRC), northwest of Lake Tanganyika and counts 609 landslides and flash flood features that occurred between the 16th and the 17th of April 2020. Many landslides are connected to the rivers where the flash floods occurred. The debris-rich flash floods inundated parts of the city (fig. 1, DRC). The terrain is characterized by an urban area, cultivated landscape, grassland, and sporadic tree cover (fig. 2d).
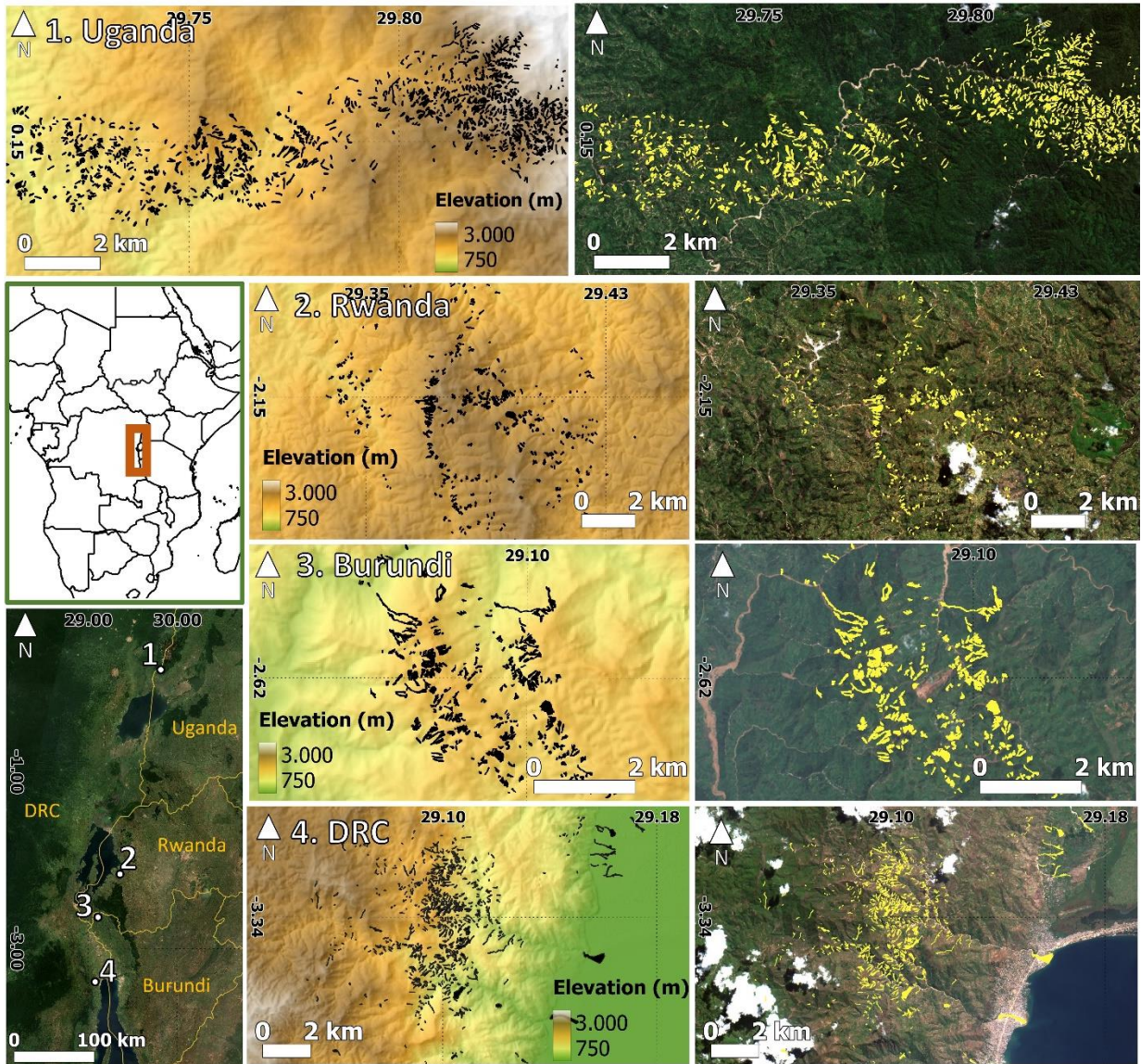
Figure 1. The location of the four GH events with their topographic (left: 30m ALOS 3D DEM, GH event features in black) and optical (right: S2 post-event image, GH event features in yellow) context. Note that in the close vicinity of the GH events of Uganda and Burundi, large sediment-loaded riverbeds are visible. This is a consequence of the GH events that contributed directly to the transport of extra material to the rivers, increasing not only their sediment content, but also their lateral mobility. These river dynamics are not included in our analysis. The two panels at the lower left depict the location of the GH

 sites (S2 imagery). Image credit: Contains modified Copernicus Sentinel data (2022), processed with

165 *Google Earth Engine. ALOS 3D DEM data provided by Japan Aerospace Exploration Agency (JAXA).*

166 The locations of the GH events (fig. 1) are derived using the Copernicus Sentinel-2 (S2) Multispectral

167 Instrument (MSI), high resolution (10m), high frequency (6 -12 days) satellite imagery. We manually

168 digitized all individual features from the first available cloud-free S2 image after the event and a cloud-

169 free S2 image with similar vegetation characteristics (compared to the post-event image) before the

170 event. We use PlanetScope Ortho Scenes (Planet Team, 2017) for validation of the GH event inventory

171 with a higher resolution satellite image. Planet operates with a constellation of multiple small satellites

172 producing very-high resolution (3m), high frequency (up to 1 day) imagery (Table 1).

173 *Table 1: Images information of manual mapping and dating GH events. Planet images are of the type*

174 *PlanetScope Ortho Scene (POS)*

GH Event	Sentinel-2				Planet	
	Date – pre	Date - post	Tile	Type	Date	Type
Uganda	2019-08-16	2020-06-01	35NRA	L1C	2020-06-29	POS
Rwanda	2018-03-09	2018-06-12	35MQT	L1C	2019-12-07	POS
Burundi	2019-08-06	2020-01-23	35MQT	L1C	2018-06-12	POS
DRC	2019-07-02	2020-06-06	35MQS	L1C	2020-10-06	POS

175 We prefer the use of Planet and S2 over the Maxar or the Spot/Pléiades images visible in Google Earth

176 because of the consistency in temporal and spatial resolution. To note, the Burundi GH event has

177 recently been mapped by Emberson et al. (2022) by means of a semi-automated method followed by a

178 manual correction using S2 satellite data. We expect our manually mapped Burundi GH event inventory

179 to be similar or more accurate since we use a combination of S2 and Planet satellite data and a

180 completely manual detection workflow. The date of GH event occurrences is determined from local

181 media and field observations, and if not available from these resources, determined by the first- and

182 last available imagery from S2 and Planet imagery.

183
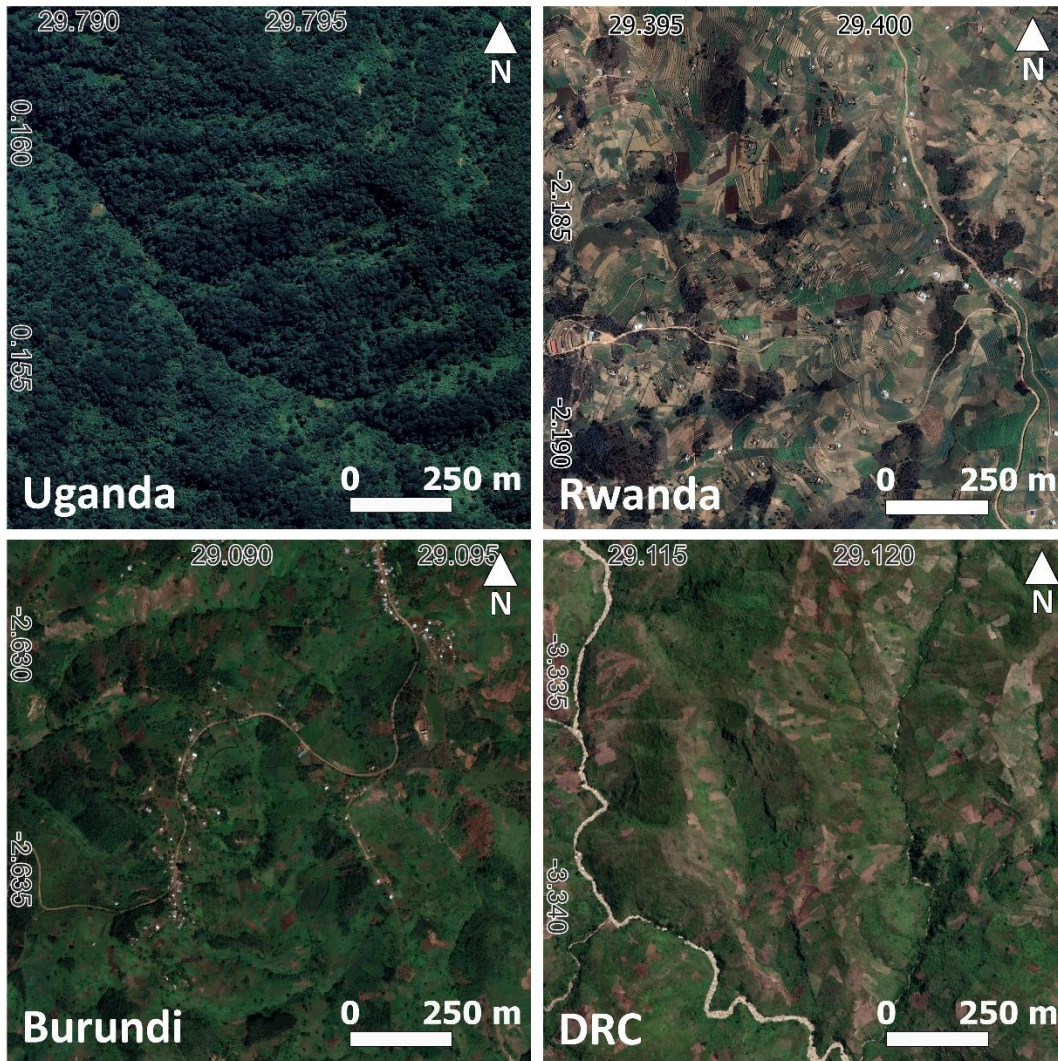
184

185   *Figure 2. Close up of the contrasting typical landscapes of the four GH events. Maps Data: Google,*
186   *©2022 Maxar Technologies (c, d) Google, ©2022 CNES/Airbus (a,b).*

2.2. SAR time series

188   SAR time series at the GH location are constructed using the Copernicus S1 Level-1 Single Look Complex
189   (SLC) imagery acquired in Interferometric Wideswath (IW). The S1 satellite is side-looking (right) and
190   operates both on the ascending (from South to North) and descending (from North to South) tracks
191   within the C-band frequency. To study the four GH events (fig. 1) we use all available high resolution
192   S1 imagery (~15x15 meter resolution) from January 2016 to January 2021 at the location of the GH
193   event at tracks 174 (ascending) and 21 (descending). This equals to between 196 and 208 ascending
194   and 120 and 193 descending images per GH event, where images occasionally overlap more than one
195   GH event. with a repeat time of six to twelve days with more consistently six days towards recent times.
196   We use both amplitude and coherence information. S1 images over the study area are provided in
197   vertical-vertical (VV) and vertical-horizontal (VH) polarizations. Different polarizations result in different
198   backscattering values (Shibayama et al., 2015, Psomiadis, 2016, Park & Lee, 2019, Burrows et al.,
199   2022). Mondini et al., 2019 noted a better definition of landslide-induced changes in vegetated areas

using the VH channel. In contrast, Burrows et al. (2022) found VV to perform better than VH for landslide event timing estimation. Psomiadis (2016) concluded that VV polarization performed better than VH polarization for flash flood mapping. Finally, VV polarization images are acquired more consistently at the locations of our GH events. We therefore decide to use VV polarization for our analysis. Due to the side-looking nature of the S1 satellite it is subjected to foreshortening, layover, and shadowing which are SAR inherent quality problems that are amplified within mountainous regions and affect image quality (Hanssen, 2001, Dzurisin, 2006). GH inventories are masked for foreshortening, layover, and shadow areas to remove the individual landslides and flash floods that fall within these inherently noisy areas.

2.3. SAR controlling factors

SAR amplitude and coherence are influenced by local slope angle (Hanssen, 2001), soil moisture (Ulaby et al., 1996, Scott et al., 2017), vegetation (Balzter, 2001, Barrett et al., 2012), and terrain roughness (Dzurisin, 2006). Coherence is additionally influenced by atmospheric changes (Rocca et al., 2000) and due to the use of image pairs, also by the temporal baseline (time between acquisition of two images), the perpendicular baseline (distance between the location of acquisition of two images) and the difference in incident angle of the paired images (Hanssen, 2001). Coherence values are generally very low (high decorrelation) in densely forested areas due to constant movement of the leaves and stems (Weydahl, 2001, Tessari et al., 2017), whereas bare soils or urbanized terrains, due to their static nature, generally reveal relatively high coherence values (Colesanti & Wasowski, 2006). An increase in coherence values after GH event occurrence is therefore expected. Amplitude values, on the other hand, show to have a quite complex reaction to terrain change. Due to the influence of soil moisture and roughness change on the amplitude values, the occurrence of a GH event could both increase and decrease the amplitude values at the location of the GH event (Mondini et al., 2021, Burrows et al., 2022). Both precipitation (in changing leaf- and soil wetness) and vegetation patterns, can dynamically influence SAR amplitude and coherence values, causing a cumulative effect on the time series (Srivastava et al., 2006, Brancato et al., 2017). This effect is more prominent over sparsely vegetated areas due to geometric (vegetation growth and farming practices) and dielectric (moisture) changes (Strozzi et al., 2000). Additionally, a change in atmosphere (precipitation events, ionospheric disturbances) can dynamically influence the coherence values (Rocca et al., 2000, Jacquemart & Tiampo, 2021). To better assess the ability to detect GH timing, it is essential to understand the dynamic factors controlling the behavior of the signal.

We derive precipitation estimates from the GPM Level 3 IMERG Final Daily (10km spatial resolution) dataset that has been validated through rain gauge data within the area (Nakulopa et al. 2022). General vegetation patterns per GH event are visualized using the Normalized Difference Vegetation Index (NDVI; Tucker, 1979). NDVI time series are derived from the Landsat-8 (30m spatial resolution) archive and processed within the GEE environment We use the Landsat 8 atmospherically corrected surface

reflectance images provided within the GEE environment. We masked them for clouds using the quality assessment band resulting from the CFmask algorithm (Foga et al., 2017).

We choose the lower resolution Landsat-8 over the higher resolution S2 imagery to reduce any unwanted local effects of NDVI change captured in the higher resolution S2 imagery, and since we are only interested in the general vegetation trends within the area this should be sufficient. From the cloud-masked images, a spatial-average NDVI time series is created spanning from 2016-2020 over the undisturbed areas of the GH event area. The NDVI time series are further processed to monthly averages, since we are interested in general vegetation patterns visible in the NDVI time series rather than changes on smaller temporal timescales.

We use the ESA Climate Change Initiative Land Cover product (ESA, 2016) to categorize GH based on their prior land cover to assess the influence of land cover on the timing detectability. This product has been validated within the region by Depicker et al. (2021), showing an accuracy of 86.1 ± 2.1% in land cover classification. All above mentioned factors are considered during the analysis of the SAR timeseries and the GH event timing estimations.

3. Methods

3.1. Sentinel-1 pre-processing

The S1 images are pre-processed using the "InSAR automated Mass processing Toolbox for Multidimensional time series" (MasTer) (Derauw et al., 2020, d'Oreye et al., 2021) processing chain (fig. 3, step 1). MasTer is a tool for automated SAR and SAR interferometry (InSAR) mass processing (Samsonov & d'Oreye, 2012, Derauw et al., 2019; 2020, d'Oreye et al., 2019; 2021), that is incremental (i.e. only computes the minimal required information when a new image is available) and optimized for mass processing. The MasTer workflow is applied on both the ascending and descending track and consists of:

(1) the application of orbit correction using the precise orbit files provided with the S1 data.

(2) The creation of time series of amplitude maps per track. Amplitude maps of each given track are co-registered on a reference image taken from that track. Every amplitude image in the radar geometry of that track is cropped and provided with the same grid and dimensions framing the area of interest. Amplitude values are calibrated to sigma nought values. The amplitude images are multi-looked by a factor 2 in azimuth and in range, to reduce speckle, leading to a roughly 28x5 m slant range resolution. Radiometric terrain correction is applied to account for the local incidence angle variating with slope angle resulting in amplitude values that are independent of slope angle (Small, 2011).

(3) The creation of coherence maps using consecutive images throughout the time series with a maximum temporal baseline of 12 days and a maximum perpendicular baseline of 150 m. The coherence maps are provided with the same multi-looking factor, grid, and ground range resolution as the amplitude images.

271   (4) All the amplitude and coherence maps from all the tracks spanning a given GH area are geocoded

272   from slant range to ground range on a common grid with a 15 by 15 m resolution using the 30 m ALOS

273   Global Digital Surface Model. We decided to geocode the SAR imagery to make it compatible with all

274   our other data products and to allow for an easier visual comparison with optical imagery.

275 **3.2. Spatial amplitude correlation**

276   We adapt the amplitude correlation approach, initially used for GH spatial detection (Mondini et al.,

277   2017, Konishi & Suga, 2018, Jung & Yun, 2020), to allow for GH timing detection at the location of the

278   GH event using the amplitude image stacks (fig. 3, step 2). We reason that the spatial correlation is

279   generally lost when the inter-pixel relationships between two images change at the location of a GH

280   event. Therefore, a significant change within the landscape such as a landslide or a flash flood will cause

281   a significant decorrelation. Due to the sensitivity of SAR amplitude to changes in vegetation (Balzter,

282   2001, Barrett et al., 2012), seasonal greening and browning trends have a pronounced influence on the

283   amplitude time series (Balzter, 2001, Barrett et al., 2012), which potentially limits the detectability of

284   the GH event within the time series. Since spatial correlation is only changing when the inter-pixel

285   relationships change, general trends that affect the entire area (lowering or increasing the SAR

286   amplitude values) do not influence the inter-pixel relationships (i.e. no spatial correlation change). Only

287   when significant inter-pixel change occurs, due to landslides or flash floods, the spatial correlation will

288   change. The spatial amplitude correlation (SAC) can therefore highlight the GH event occurrence within

289   the time series, while reducing the seasonal dynamics. To calculate the SAC, we use equation 1 that we

290   adapted from Jung & Yun (2020).

291    $$SAC_{x,y,poly} = \frac{\sum\{(A_{r,poly} - \overline{A_{r,poly}})(A_{x,poly} - \overline{A_{x,poly}})\}}{\sqrt{\sum\{(A_{r,poly} - \overline{A_{r,poly}})^2\}\sum\{(A_{x,poly} - \overline{A_{x,poly}})^2\}}} \quad x = date_1 \dots date_{N+1}; x \neq r \qquad (1)$$

292   with $SAC_{x,r,poly}$ the spatial amplitude correlation for the impacted area of date x in reference to date r,

293    $A_{x, poly}$ the amplitude pixels of impacted area at date x, and $A_{r, poly}$ the amplitude pixels of impacted area

294   at reference date r. Instead of calculating correlation between two subsequent images over a given

295   window, we calculate the correlation using one reference image (A_r) and all the other images within the

296   time series (A_x) using only the pixels within a designated impacted area (e.g. single GH feature or

297   complete GH event) ($_{poly}$). Consequently, every image within the amplitude image stack can be used as

298   a reference image and due to slight changes within every amplitude image this will inevitably result in

299   different SAC time series, one better highlighting the GH event than the other. We apply the equation

300   separately for ascending and descending images in a parallel workflow. Figure 4 shows schematically

301   how the SAC time series should behave using different reference images. Taking a reference amplitude

302   image before the GH event occurrence (fig 4a), results in high SAC before and low SAC after GH event

303   occurrence. The opposite is expected when using a reference amplitude image after the GH event (fig

304   4b).

305 We use every available image within the amplitude image stack as a reference image and calculated

306 the respective SAC time series from it. From here, it is necessary to identify the most appropriate

307 reference image.

308
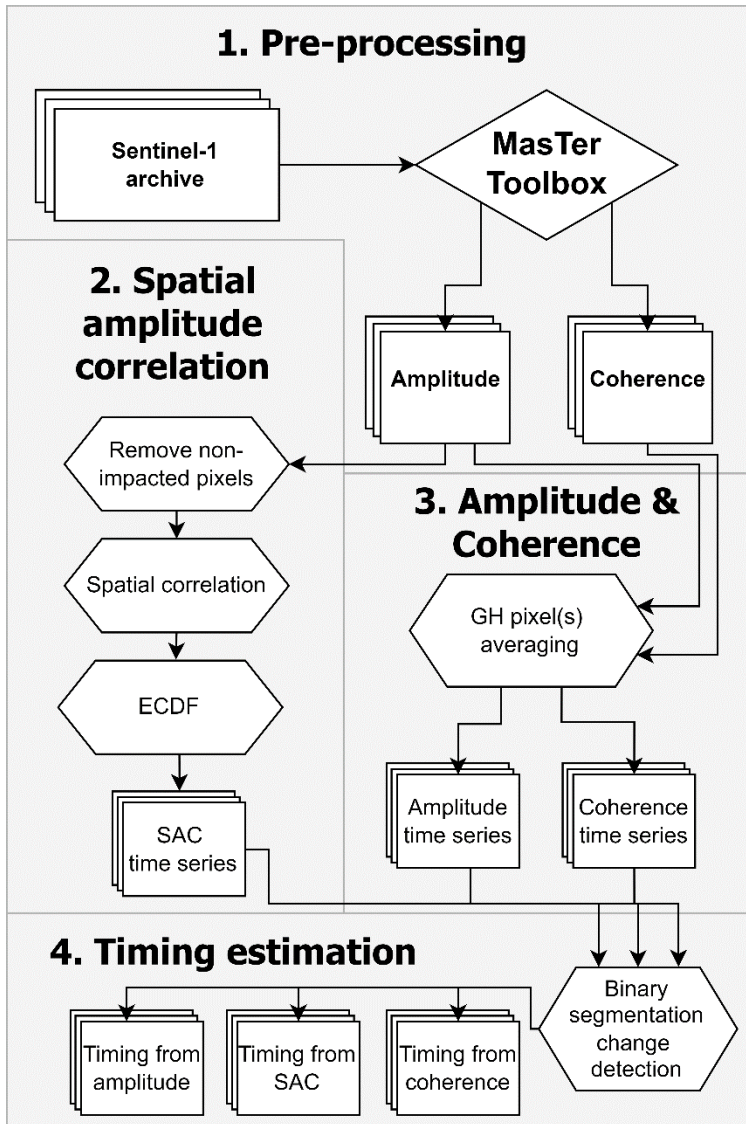
309

310 *Figure 3. Flowchart of the four-step methodology. Rectangles represent initial input imagery, output*

311 *image stacks or time series products. The rhombus represents the external software product. Hexagons*

312 *represent methodological steps, which are described in the text. (1) Pre-processing of the S1 imagery*

313 *using the MasTer processing chain to acquire amplitude and coherence image stacks. (2) Application of*

314 *the spatial amplitude correlation (SAC) method using Empirical Cumulative Distribution Functions (ECDF)*

315 *on the amplitude image stack resulting into SAC time series. (3) GH pixel(s) averaging for every image*

316 *in the amplitude and coherence image stacks resulting into amplitude and coherence time series. (4)*

317 *Application of binary segmentation change detection to acquire the date of the most significant change*

318 *within the amplitude, SAC, and coherence time series.*

319   Hence, we develop a new methodology that identifies the most suitable reference amplitude image by
320   finding the SAC time series that most distinctively shows changes related to the GH event occurrence.
321   We distribute every SAC time series as Empirical Cumulative Distribution Functions (ECDF) resulting in
322   multiple ECDF curves equal to the amount of reference images. A SAC time series that contains a distinct
323   change indicative of the GH event occurrence will show a similar distinct change in its ECDF.
324   Contrastingly, SAC time series that fail to distinctively highlight the GH event, show an ECDF that is
325   similar to a normally distributed ECDF. Therefore, we create a normally distributed ECDF, using the
326   mean and standard deviation derived from the ensemble of ECDF curves, and identify the ECDF that
327   deviates most from it. Per ECDF we calculate and cumulate the difference from the normally distributed
328   ECDF. The ECDF with the highest cumulative difference is chosen as most representative and the related
329   SAC time series was used.

330   **3.3. Geomorphic hazard event timing estimation**

331   GH event timing is determined on two scales within separate workflows:

332   - Timing workflow 1: the complete GH event scale. In this workflow, the steps outlined in figure
333   3 are carried out once using all pixels encompassing the full GH event. This results in one
334   ascending and one descending track time series for amplitude, SAC, and coherence.
335   - Timing workflow 2: the individual GH scale. In this workflow, the GH event is subdivided in
336   multiple individual GH features and the steps outlined in figure 3 are carried out separately for
337   each individual GH feature. This results in multiple ascending and multiple descending track
338   time series, equal to the amount of individual GH features, for amplitude, SAC, and coherence.

339   In both workflows we do not choose to remove fuzzy pixels (i.e. edge pixels that contain both impacted
340   and non-impacted landscape), since we do not know the effect of these pixels on the SAR time series
341   and GH event timing estimations. This allows us to establish baseline results. The ascending and
342   descending track data are processed separately throughout the two workflows. Amplitude and
343   coherence time series are generated by averaging the values within the identified impacted area per
344   image (fig 3, step 3) and the SAC time series are generated by applying the SAC method (fig 3, step 2;
345   section 3.2) within both workflows. The resulting time series are normalized using the time series
346   average to improve comparability.

347   Additionally, we make an effort to remove the seasonal influence and atmospheric effect on the
348   amplitude and coherence time series by subtracting the regional amplitude and coherence trend (i.e.
349   time series) from the GH event scale amplitude and coherence time series (timing workflow 1). Both
350   precipitation events and seasonal vegetation dynamics are expected to cover the complete GH event
351   and its surrounding area. This detrending will therefore emphasize the change induced by the GH event
352   occurrence while removing any regional changes induced by either seasonal vegetation dynamics or
353   atmospheric effects (e.g. Jacquemart & Tiampo, 2021). The regional amplitude and coherence time
354   series are established by following step 1 and 3 in the methodology flowchart (fig. 3), using a larger

area surrounding the GH events as input (i.e. a square of approx. 1.5 times the GH event area, excluding the exact location of the GH event). This results in the detrended amplitude and detrended coherence data products. SAC is created to already consider seasonal vegetation dynamics so no additional detrending for this data product is performed.

We decide not to detrend individual GH feature time series (timing workflow 2), which could include the use of a detrending buffer (e.g. Burrows et al., 2022). Since we deal with complex heterogenous land cover, proximate land cover does not necessarily represent the land cover at the GH feature, which prohibits from accurate detrending. Additional research is required before implementing such a method within a wide variety of environments.

Timing is defined on every time series (for amplitude, SAC and coherence) using a binary segmentation change detection approach (Bai, 1997, Fryzlewicz, 2014) using the python package 'Ruptures' (Truong et al., 2020) (fig. 3, Step 4). The algorithm was set to predict only one breakpoint since we aim to detect the most significant change in the time series. The output of the applied binary segmentation change detection algorithm is a value that represents the location of an image within the image stack. The date of this image is extracted and assigned as the earliest date after the GH event occurrence. This applies for the amplitude and SAC time series. However, since coherence is based on image pairs, it would identify the image pair right after the GH event. We therefore assign the first date from this image pair as the earliest date after the GH event occurrence. On the complete GH event scale (timing workflow 1) this results in two dates (from ascending and descending track) per data product (amplitude, detrended amplitude, SAC, coherence, detrended coherence). On the individual GH scale (timing workflow 2), this results in several dates, equal to two times (one for ascending and one for descending track) the amount of individual GH features per data product (amplitude, SAC, coherence). Here we identify the date that occurred most frequently (majority) as representing the timing of the event. We define the minimal uncertainty in timing estimation by the difference between the estimated date of occurrence and the date of the image prior to that (i.e. a maximum of 12 days).

380
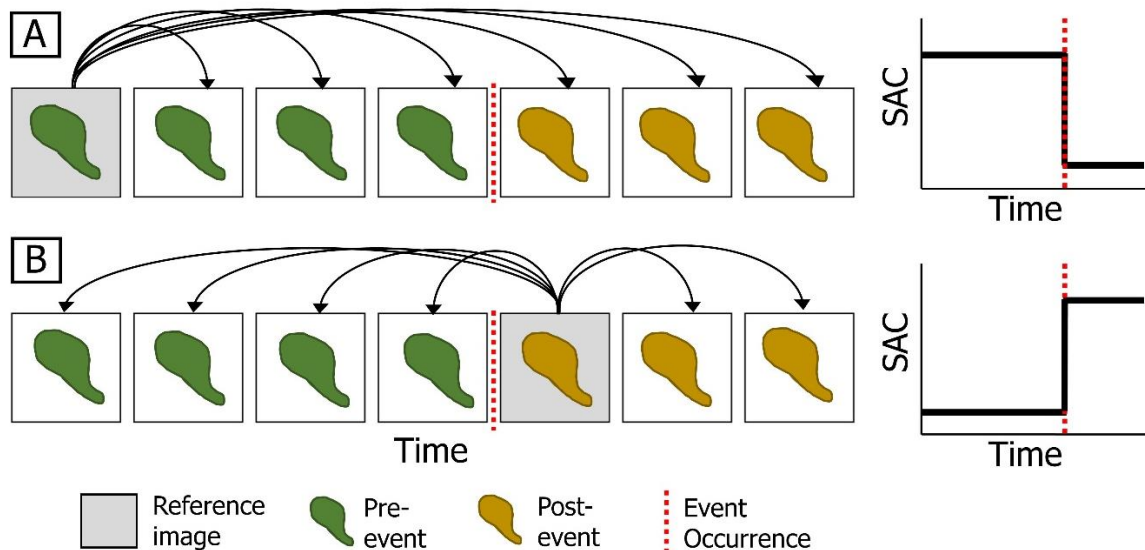
Figure 4. Idealized schematic of the SAC method using two different reference images: one before and one after the occurrence of the GH event (A, B). Squares represent images, the red dotted line indicates the occurrence of a GH event. Inside the images are the conditions of the impacted area (represented here as single GH feature but is similar for complete GH event). Pre-event conditions are displayed in green. Post-event conditions are displayed in brown. The black curved lines represent the combination of images on which equation 1 is applied to achieve the resulting SAC time series. The schematic SAC graphs (right) depict the expected results using a reference image before the event (A) with high correlation before and low correlation after the event, and using a reference image after the event (B) with low correlation before and high correlation after the event.

3.4. Sensitivity analysis with respect to landscape characteristics

In section 2.3 we discuss the controlling factors on the SAR signal. Here, we aim to understand the influence of these controlling factors plus the influence of individual GH properties on the detectability of the event timing. We carry out a sensitivity analysis on GH area (effect of a changing number of pixels/pixel mixing, Deijns et al., 2020), slope angle (change in image acquisition geometry, Zebker & Villasenor, 1992, Hanssen, 2001), land cover (changing vegetation and soil moisture patterns, Giertz et al., 2005), and slope aspect (different effect of layover, shadowing within ascending and descending track, Hanssen, 2001, Dzurisin, 2006). We carry out the analysis separately for the ascending and descending track images. Per individual GH feature we derive the average value of the above-mentioned parameters. We find more smaller-sized GH in the Rwanda GH event (fig 5a), a slight deviation (peak more to the left) in slope distribution for the Uganda GH event (fig. 5b) and a large variation in slope aspect distribution for different GH events (fig. 5d). Additionally, land cover distribution is different for every GH event (fig. 5c) which corroborates with what we see in figure 2.

The sensitivity analysis is carried out iteratively over every parameter from a minimum value to a maximum value using predefined steps (Area: 1000 m^2, Slope: 5°, Land Cover: per individual land cover

type, Slope aspect: 45°). Per iteration the GH inventory is reduced to contain only individual GH features that meet the iteration conditions. We exclude bins that contained less than 20 individual GH features to avoid non-sense (very high or very low) values that would negatively influence the quality of the trend.

Per bin-size, we calculate the timing for every individual GH feature, and the percentage of timing estimates that fall within one month of the actual event occurrence over the total amount of individual GH features. Higher percentages indicate more timing estimates closer to the actual event occurrence. The variations within this percentage are subsequently analyzed to relate changing characteristic to performance.
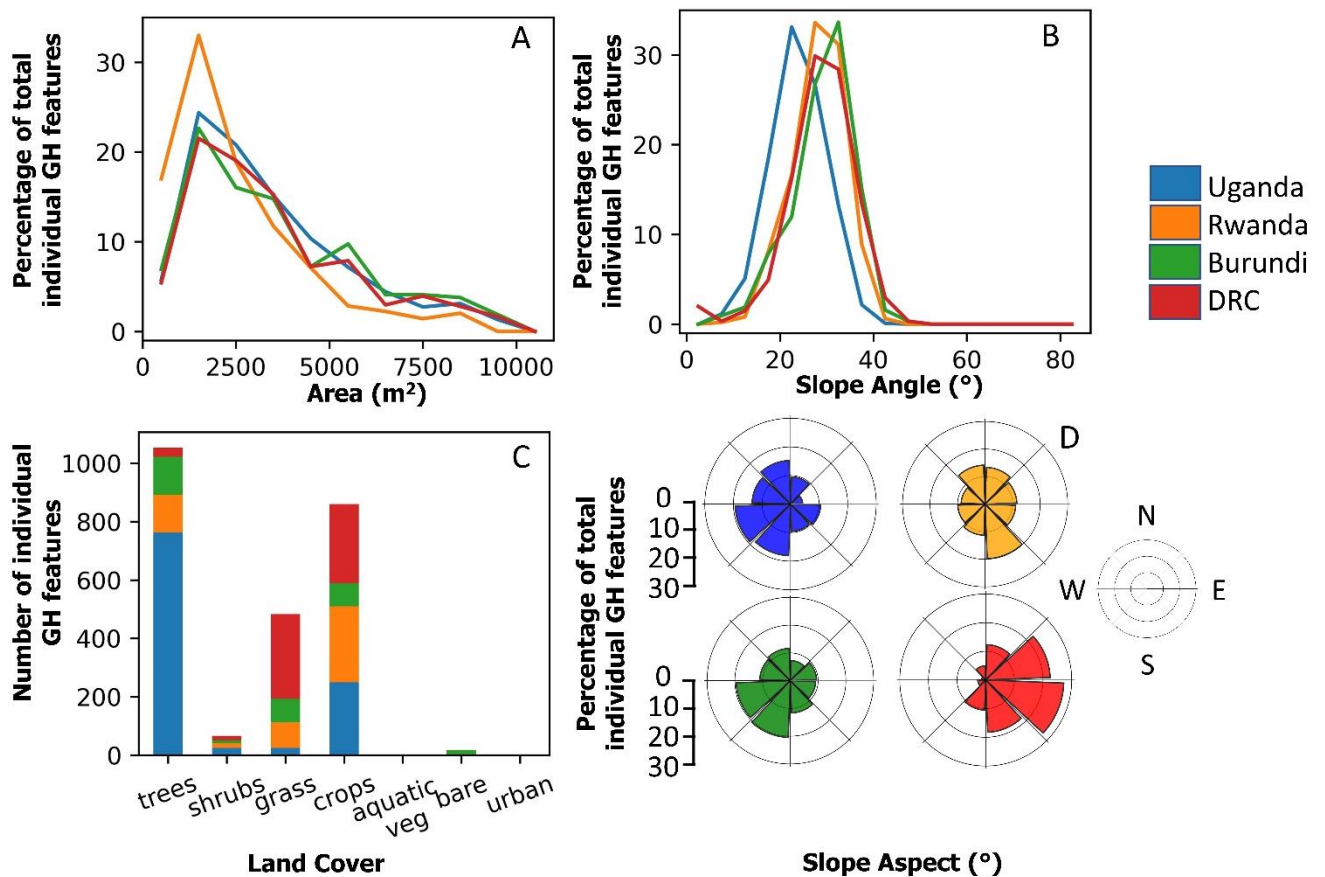
Figure 5. Parameter distributions per GH event (Uganda, Rwanda, Burundi, and DRC). (A) Percentage of individual GH over total amount of individual GH against area (m^2), bins of 1000 m^2. (B) Percentage of individual GH over total amount of individual GH against slope angle, bins of 5°. (C) Number of individual GH against land use/land cover. (D) Percentage of individual GH over total amount of individual GH against slope aspect, bins of 15°.

4. Results

4.1. Geomorphic hazard event time series

We created amplitude, detrended amplitude, SAC, coherence, detrended coherence time series for the four GH events in Uganda, Rwanda, Burundi, and DRC (location in fig. 1) and present it in figure 6 together with the average monthly Landsat 8 NDVI and IMERG monthly cumulative precipitation.

The distinctiveness of the GH event occurrence within the time series varies significantly per data product (fig. 6). SAC (fig. 6i-l) and coherence (fig. 6m-t) time series showcase the timing of the event with a significant change of value at the time of the event occurrence. A significant decrease in co-event (the coherence value from the pre- and post-event image) coherence is not visible.

The amplitude time series do not show any distinct change at the time of the GH event occurrence (fig. 6a-h), except for the Uganda GH event (fig 6a,e). Particularly in the amplitude time series, and to a minor extent in the coherence time series, clear cyclicity can be observed, that correspond with the two drier periods (December-February and June-August) that are prevalent in the region (Bonfils, 2012, Nicholson 2017, Monsieurs, 2018a). The NDVI shows seasonal correlation with the precipitation patterns, where NDVI patterns follow precipitation patterns with a short time lag (fig 6u-x). Stronger NDVI variations align with a stronger cyclicity within the amplitude, SAC, and coherence time series which is particularly visible when comparing the Uganda GH event (weak amplitude SAC and coherence cyclicity, limited NDVI fluctuations) and the DRC GH event (stronger amplitude, SAC, and coherence cyclicity, large NDVI fluctuations). The cyclicity clearly influences the distinctiveness of the GH event within the time series. When comparing the landscape of both GH events (fig. 2a,d) a sharp contrast is observed. The Uganda GH event region is mostly covered by forest, whereas the DRC GH event region is mostly covered by grass- and cropland. Consequently, we find that seasonal NDVI oscillations vary significantly from one study area to another given the difference in landscape.

Time series detrending clearly reduces seasonal cyclicity within the time series, which is particularly visible for the coherence time series (fig. 6q-t) and to a much smaller degree for the amplitude time series (fig. 6e-h). For example, the DRC GH event coherence time series benefits from this detrending procedure such that seasonal cyclicity is almost completely removed, leaving a distinct increase in coherence values after the occurrence of the GH event (fig. 6t). Detrending the amplitude time series shows a minor reduction in cyclicity, but the distinctiveness of the GH event within the time series remains low.
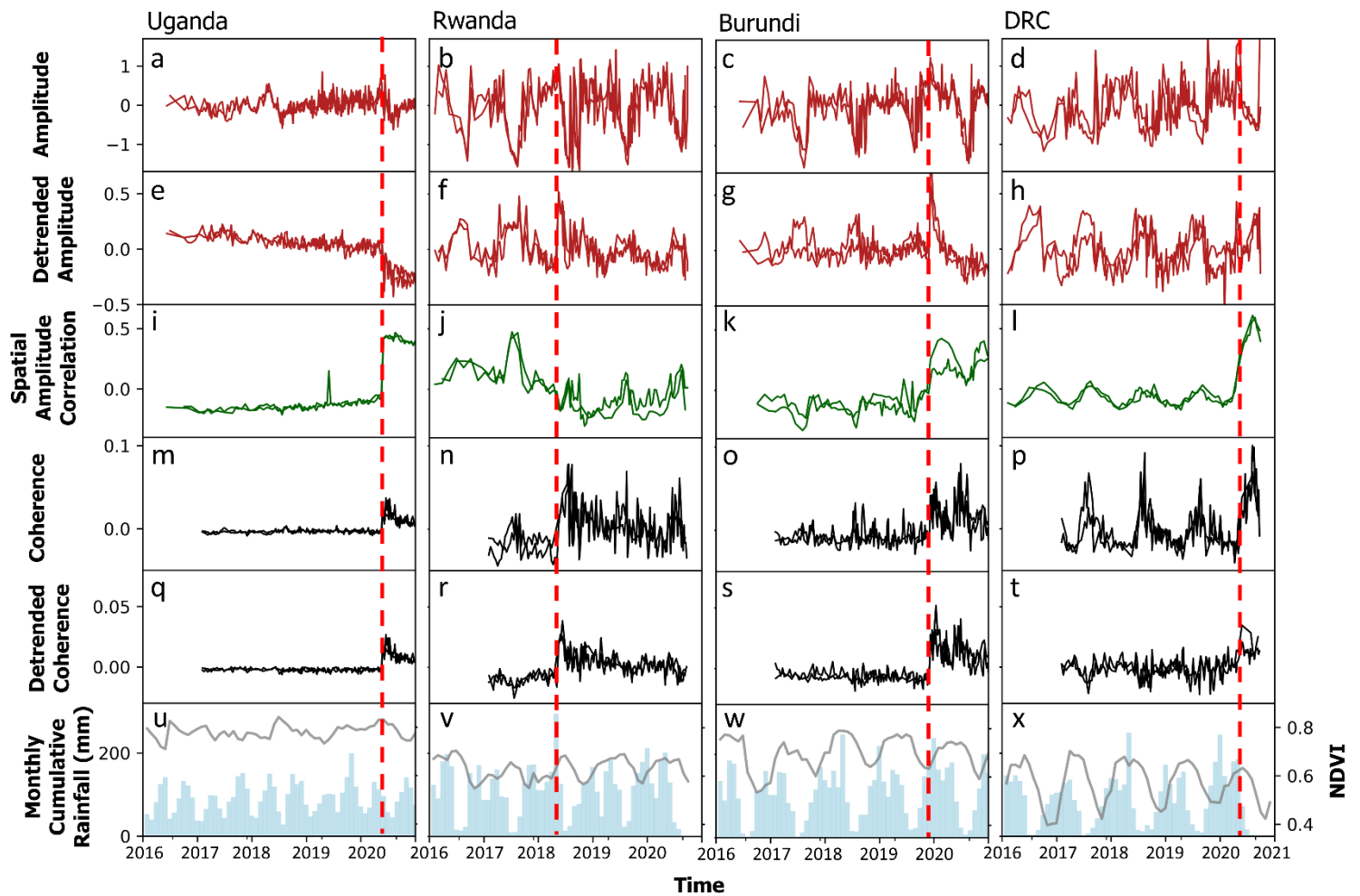
Figure 6. GH event (detrended) amplitude (red), spatial amplitude correlation (SAC, green) and (detrended) coherence (black) time series. The dashed red line represents the timing of the GH event occurrence within the time series. All coherence, amplitude and SAC time series show two lines of a similar color representing the ascending and descending track time series. The time series are created according to the complete GH event scale workflow described in sections 3.3. The bottom row shows the monthly cumulative precipitation (light blue bars) from IMERG satellite data and the monthly averaged NDVI values (grey line) from Landsat 8 (method described in section 2.3).

4.2. Geomorphic hazard event timing

Figure 7 shows the timing estimation at the GH event scale (timing workflow 1) from the (detrended) amplitude, SAC and (detrended) coherence time series. The difference in days from the actual occurrence of the GH event is visualized by a range that incorporates the minimal uncertainty in timing estimation (fig. 7 and fig. 8; see section 3.3). Timing estimations from the amplitude time series generally have lower accuracies with estimated timing ranging from a 46 day difference (Uganda, descending) to a 1000 day difference (Uganda, ascending). Estimations from the SAC time series range between a 1 day (Uganda) and an 85 day (Rwanda) difference and estimations from the coherence time series range between a 1 day (Uganda) and a 47 day (Rwanda) difference. Highest accuracies are

achieved with time series showing less seasonal fluctuation and a steep change at the time of event occurrence (fig. 5). Timing estimations from the detrended amplitude time series show an increased accuracy compared to amplitude time series with the most significant change for the Uganda GH event from a 46-1000 to a 13-22 day difference, but performance is still poor and generally useless for accurate timing estimation. Detrending the coherence time series increases timing estimation accuracy compared to the non-detrended coherence timing estimation for the DRC event (25-32 to a 1-5 day difference), but in general the estimations remain the same.

Figure 8 shows the timing estimation based on the individual GH features within the GH event (timing workflow 2). Here, the estimated timing represents the date that is estimated most frequently between all individual GH features (as explained in section 3.3). The percentage of individual GH features that estimate this (most frequently estimated) date over the total amount of GH features (%maj) are shown in figure 8.

In general, timing estimation from the amplitude time series have low accuracies with estimated timing ranging from a 13 day difference to an 831 day difference. A distinct increase in accuracy is seen for the Uganda GH event compared to the GH event scale (fig. 7) However, the other GH events do not show any distinct increase in timing estimation accuracy. The %maj ranges between 13% and 32.4% and shows that for some GH events a large portion of the individual GH features estimate a date that is far from the actual date of the GH event occurrence. The percentage of individual GH features that estimate a date within one month of the actual GH event occurrence from amplitude time series is 24.2% (ascending) and 26.9% (descending) for the Uganda GH event, but much lower for the other GH events, corroborating the fact that the timing detection method performs poorly for the amplitude data product.

Timing estimations from the SAC time series from individual GH features (fig. 8) differ compared to the timing estimations at the GH event scale (fig. 7). An increase in accuracy is seen for Rwanda (ascending) and DRC (ascending) and a decrease in accuracy for Burundi (ascending) and DRC (descending). The estimated timing ranges from a 1 day difference to an 85 day difference. Although estimated timing accuracy is higher for SAC compared to amplitude, %maj values are quite low, indicating weak estimations. The percentage of individual GH that estimate a date within one month of the actual GH event occurrence ranges from 0.2 (Rwanda, descending) to 38,1 (Uganda, descending). Exceptionally, for the Uganda GH event, %maj and estimated timing within one month of the GH event occurrence from the SAC time series is highest in comparison with amplitude and coherence (fig. 8).

Timing estimations from the coherence time series from individual GH features (fig. 8) are similar to those achieved at the GH event scale (fig. 7), and have, generally, the highest accuracy for all data products. The %maj values ranged from 13.5 (Burundi, ascending) to 38.4 (DRC, descending). The percentage of individual GH features that estimates a date within one month of the actual GH event occurrence ranges from 0 (Rwanda, descending) to 38,4 (DRC, descending). The low percentages from

502 the Rwanda descending track can be attributed to the fact that the estimated date is 37 days from the
503 GH event occurrence and therefore just falls outside the one-month threshold.

504
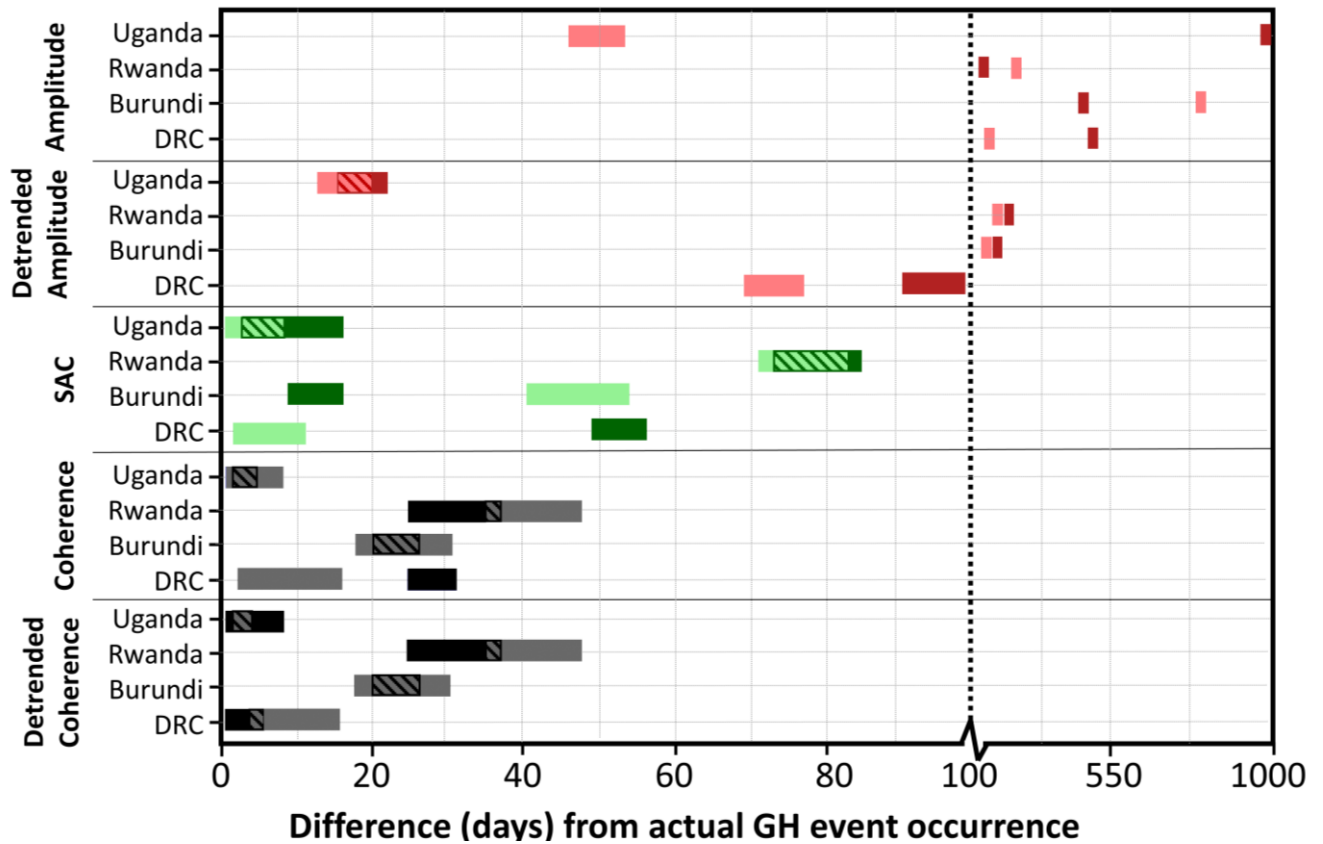
Figure 7. Estimated GH event timing using the complete GH event scale (workflow 1) for amplitude, detrended amplitude (red), SAC (green), coherence and detrended coherence (black). The darker colored bar representing the ascending track results. The lighter colored bar representing the descending track results. The length of bars represent the uncertainty in timing (see section 3.3). Dashed lines on the bars represent the overlap between the ascending and descending track results.
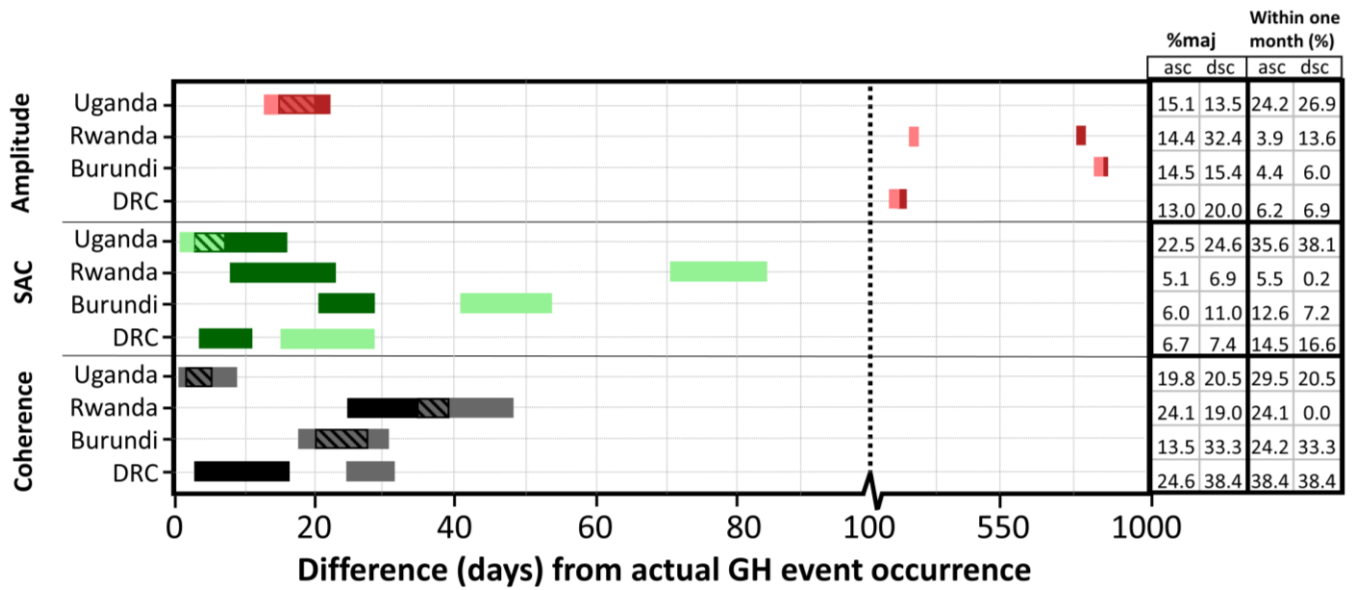
510

511 *Figure 8: Estimated timing from the individual GH feature scale (workflow 2) for amplitude, detrended*

512 *amplitude (red), SAC (green), coherence and detrended coherence (black). The darker colored bar*

513 *representing the ascending track results. The length of bars represent the uncertainty in timing (see*

514 *section 3.3). Dashed lines on the bars represent the overlap between the ascending and descending*

515 *track results. In the %maj column we present the percentage of individual GH features over the total*

516 *amount of individual GH features that were included in the majority vote separated for the ascending*

517 *(asc) and descending (dsc) track. In the 'within one month' column we present the percentage of*

518 *individual GH features over the total amount of individual GH features that estimated a date within one*

519 *month of the actual event occurrence.*

520 **4.3. Sensitivity analysis with respect to landscape characteristics**

521 GH size seems to have a clear influence on time estimation accuracy. Specifically, the SAC and coherence

522 show a clear increase in percentages of estimated timing within one month of the GH event occurrence

523 with increasing GH size (fig. 9 a-f). R^2 values show a relatively reliable fit for both SAC and coherence.

524 Amplitude shows a slight increasing trend, but associated R^2 values are non-significant.

525 Slope trend lines (fig. 9 g-l) show in general little to no inclination and R^2 values are non-significant,

526 except for the coherence ascending track. Here, a clear increase in slope angle becomes visible with a

527 comparatively higher R^2 (although clearly less significant than R^2 from the GH size analysis).

528 To assess the general influence of land cover on the ability to estimate GH event timing we combined

529 both the ascending and descending track results for all four GH events in each boxplot (fig. 9 m-o).

530 Each boxplot therefore contains a total of eight data points per land cover type. The major land cover

531 classes within the GH events were tree covered area, grassland, and cropland (Fig 4d). Median

532 percentage values range around 9-10 % for amplitude, 11-16 % for SAC, and 27-34 % for coherence.

533 Although median values within the grassland land cover type seem to be systematically higher among

the three data products (amplitude, SAC, and coherence), differences with other land covers are quite small. No specific land cover shows a significant better performance.

To assess the influence of the slope orientation, we derive the difference between ascending and descending track percentages per bin and determine which track shows better performance (fig. 9p-s). At the results for the Rwanda GH event (fig. 9q) we see for SAC and coherence an all-round favorability for the ascending track, that can be explained by the fact that, like the results in figure 8, the Rwanda GH event had almost no estimations within one month of the GH event occurrence for the descending track. The results presented for Uganda, Burundi and DRC GH events (fig. 9p,r,s) show a general favorability of the ascending track for individual GH features that have an aspect of approximately 45-180°, whereas a general favorability of the descending track for individual GH features that have an aspect of approximately 225-360°. In contrast to this general trend, the opposite seems to be visible for the Uganda GH event coherence.
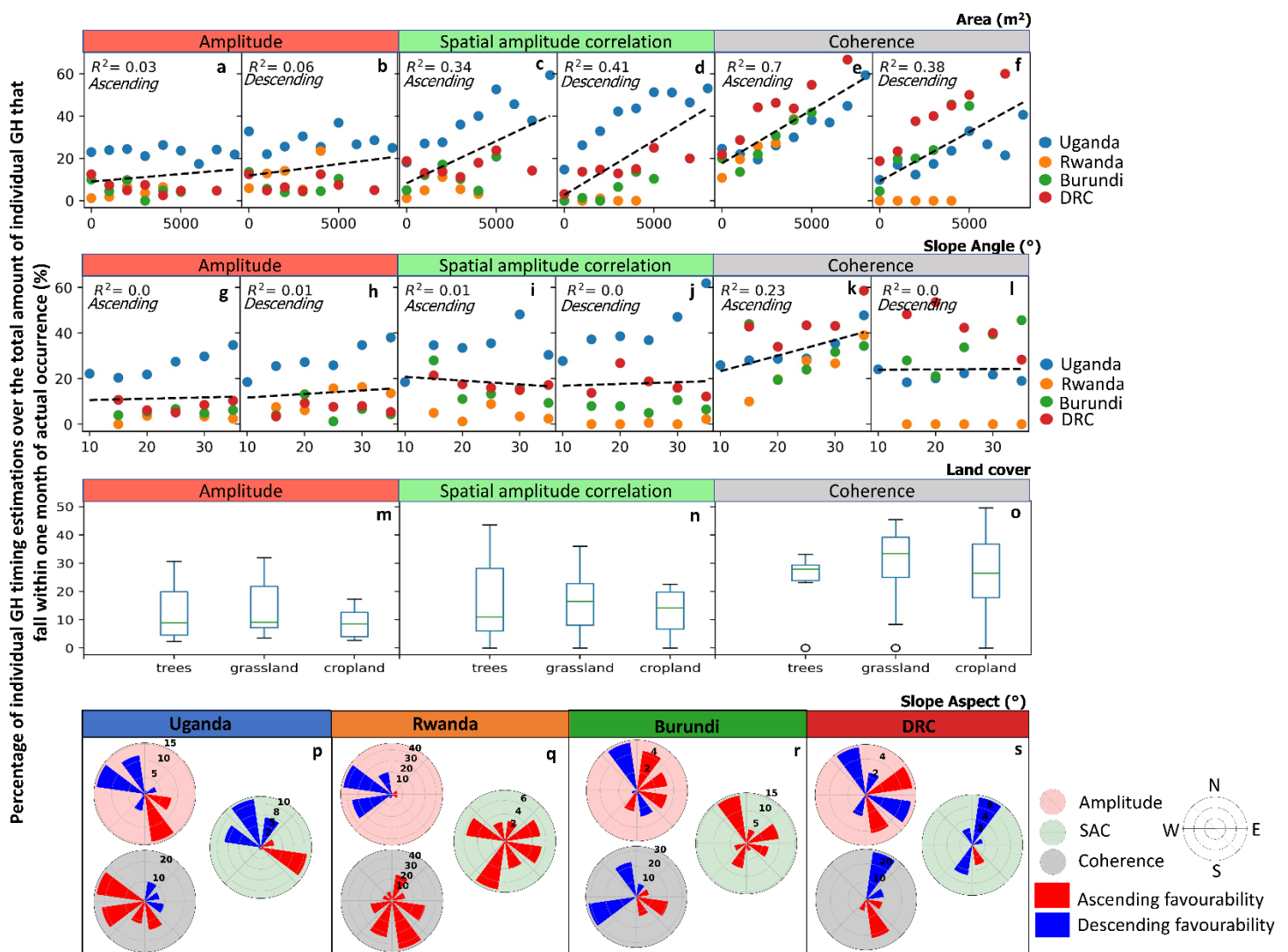
Figure 9. Timing estimation performance over changing individual GH feature area (a-f), slope angle (g-l), land cover (m-o) and slope aspect (p-s). The y-axis displays the percentage of individual GH features

that estimated a timing that falls within one month of the actual GH event occurrence over the total amount of individual GH features per GH event. Bin sizes: area=1000m, slope angle=5°, slope aspect=45°. Area (a-f) and slope angle (g-l) plots are separated per track, and the colors indicate the different GH events. The black dashed lines present the linear trend lines fitted to the data (a-l) for which the associated R² values are included. Land cover (m-o): boxplots give lower and upper quartiles and median. The whiskers of each box represent 1.5 times the interquartile range. Outliers beyond whiskers are shown as dots. Slope aspect (p-s): the polar plots present the favorability of the ascending (ASC) or descending (DSC) track per slope aspect (see section 4.3). The color of the polar plot background indicates the SAR data product.

5 Discussion

In this study we present a regionally applicable methodology to automatically determine GH event timing using S1 SAR data. Our study improves on the recent advances in GH event timing estimation research as: (1) we are one of the firsts to use amplitude, SAC and coherence time series in a systematic manner to detect the timing of GH events (Mondini et al., 2021), (2) we defined a methodology where no prior knowledge of the GH event timing is required, (3) we applied our methodology on contrasting landscapes and (4) we combined, for the first time, landslides and flash floods in a single detection approach. Here we discuss our insights, results considering recent developments, and the potential improvements and future perspectives of our methodology.

5.1. Insights in geomorphic hazard event timing estimation from SAR

5.1.1 Geomorphic hazard event timing estimation

The use of amplitude or detrended amplitude time series in our methodology does not prove to be an effective approach to accurately determine the timing of GH events since it gives an estimation accuracy of 13 to 1000 days with the actual time occurrence of the events. A clear increase in accuracy is obtained from SAC with an accuracy of 1 to 85 day. However, the most accurate results are achieved with coherence and detrended coherence with a 1 to a 47 day accuracy.

GH event timing accuracies are higher for GH events that occurred in remote areas with low amounts of cultivation and human influence (highest accuracies for Uganda GH event, lowest for Rwanda GH event). The magnitude of the seasonal vegetation oscillations, which shows connectivity with the precipitation patterns (fig. 6), varies significantly with changing landscapes and results in profound seasonal cyclicity in both the amplitude and coherence timeseries. Although the coherence is additionally influenced by atmospheric effects (Rocca et al., 2000), the influence of both the vegetation and atmosphere on the coherence does not obscure the GH event induced change within the time series. Notably, after detrending, the effects of both seem to be almost negligible. Denser and taller vegetation, result in lower seasonal cyclicity within the amplitude and coherence time series. S1 operates in C-band frequency, meaning that the emitted signal penetrates the canopy layer and subsequently bounces on the branches, and leaves underneath (Dzurisin, 2006). A reduction in vegetation after a seasonal dry

584 period within sparsely vegetated areas, i.e. the grass- and croplands in the DRC GH event, will likely
585 expose the soil underneath and have a pronounced influence on the backscattering signal given the
586 difference in backscattering properties of vegetation and soil (Strozzi et al., 2000, Weydahl, 2001,
587 Colesanti & Wasowski, 2006, Tessari et al., 2017). In contrast, a seasonal dry period in a dense forest,
588 (i.e. Uganda GH event) would affect the density of the canopy cover. However due to the height and
589 close vicinity of the vegetation to each other a dry period does not necessarily lead to more soil
590 exposure. This is corroborated by the fact that the NDVI does not change much for the Uganda GH
591 event, despite the seasonal patterns in precipitation (fig. 6). The regions that are covered with the
592 denser and most uniform vegetation are commonly environments with the lowest chance of getting
593 timing information from other sources (media, citizen-observer networks) as compared to GH events in
594 more inhabited landscapes (Jacobs et al., 2019, Monsieurs et al., 2019).

595 The complex reaction of the SAR signal to soil moisture and roughness change can causes both an in-
596 and decrease of the amplitude at the same GH event location (Mondini et al., 2021, Burrows et al.,
597 2022). Next to the seasonal influence (fig. 6), this can also be a potential reason why no significant
598 changes at the timing of the GH event are distinguished for all GH events. The inter-pixel variation
599 captured in SAC proves to be a good tool to account for both this potential in- and decrease and any
600 seasonal variation in amplitude values at the location of the GH event and increased timing estimation
601 accuracy.

602 The pre-event, co-event, and post-event coherence values of our four GH events correspond with the
603 study of Tzouvaras et al. (2020), where a distinct difference in pre- (low) and post- (high) GH event
604 coherence values is observed at the location of a landslide occurrence. We observe the same patterns
605 with the GH events that contain flash floods, likely because a clear landscape change is observed after
606 the occurrence of the (often sediment-rich) flash floods (fig. 1). The co-event coherence drop as
607 observed by Tzouvaras et al. (2020) and Burrows et al. (2019) at the location of a landslide occurrence
608 does not prove to be significant enough to be able to determine GH event timing. This is most likely
609 attributed to the fact that the GH events occurred in low-coherence (vegetated) areas (Weydahl 2001,
610 Tessari et al., 2017).

5.1.2 Geomorphic hazard event distribution

612 An increase in GH area improves the accuracy of timing detection, which can likely be related to the
613 increased number of pixels fully covering the GH feature relative to the fuzzy edge pixels (e.g. Foody
614 and Mathur, 2006, Deijns et al., 2020, Zhong et al., 2021).

615 Generally, accuracy is not correlated with slope angle (fig. 9). However, an increase in accuracy with
616 increasing slope with a relative low reliability is observed for coherence. Nevertheless, this trend must
617 be considered with a certain caution: (1) the trend is dependent on the quality of terrain correction
618 during the pre-processing step (section 3.1), which should make SAR values independent of slope angle
619 (Small, 2011), (2) a changing slope angle could influence the GH size (Chen et al., 2016), (3) we take

620 the average slope angle per GH. Elongated GH features (mainly the flash flood features in the GH
621 inventories) will have an average slope angle that is not representative for every part of the GH.

622 Although a clear difference can be observed in time series response to GH events located in different
623 landscapes (fig. 6), the comparison with the land cover does not allow to find a clear relationship with
624 the type of vegetation (fig. 9). Since the land cover distribution is not equal amongst GH events (fig.
625 5), the results are, for some GH events, based on a low amount of individual GH features. The general
626 trends could therefore also be influenced by additional underlying trends such as GH size and GH slope
627 angle. The observed large variation in values per box plot (fig. 9m-o) might be an indication of this.

628 By using the right-looking S1 satellite data, foreshortening, and layover effects should be limited with
629 descending track acquisitions for GH exposed towards the west (180-360°) and with ascending track
630 acquisitions for GH exposed towards the east (0-180°). The shadow affects in the opposite direction
631 and is dependent on the slope of the terrain (Bamler, 2000). We see that, generally, the individual GH-
632 features on the descending slope tend to have a higher timing estimation accuracy for the west facing
633 slopes and the individual GH features on de ascending track for the east facing slopes, which is as
634 expected. However, there remains variability in the result, for example, an opposite pattern is visible
635 for Uganda GH event with the coherence and a partial favorability for the descending track acquisition
636 on east facing slopes is visible for the DRC GH event. Future research on the detailed effect of changing
637 GH feature aspects on the ascending and descending SAR time series can provide additional valuable
638 information in this context.

639 Our derived trends are established from GH events with each 318 to 1063 individual GH features and
640 provide a good indication of the SAR response to changing landscape parameters. It remains interesting
641 to see if these trends sustain with the addition of more GH events from different landscapes.

642 **5.2. Result considering recent developments in SAR timing detection**

643 Our results are somewhat in contrast with Burrows et al., (2022), who argue that coherence is less
644 performant than amplitude for GH event timing. Using amplitude data, they were able to estimate the
645 timing of ∼ 30% of landslides per inventory with an accuracy of ∼80% and an average precision of 12
646 days. Whereas by using coherence (60x60m resolution) they acquired much less accurate results (24-
647 47% correctly estimated). Their study, however, differs in several aspects from our analysis:

648 1. Burrows et al., (2022) applied their method with a pre-defined notion of GH event timing, i.e. known
649   year and season. For our GH events, we see distinct seasonal dynamics mainly within the amplitude
650   time series. Zooming in on a specific time frame (3 months before and 3 months after the GH event
651   occurrence like Burrows et al. (2022)) reduces the overall seasonal dynamics, which could be the
652   cause of a wrongly identified GH event change. Reducing this time window will potentially improve
653   the detectability of the GH event within the time series. However, our methodology is intended to
654   be applicable in areas such as the western branch of the East African Rift, an area characterized by
655   data scarcity (Dewitte et al., 2021). In areas like these, information on the temporal distribution of

GH events may not always be available. We therefore defined a methodology that requires no knowledge on GH event timing before application, which is an advantage if no GH event timing is present, however, this increases the chance of any seasonal influence visible within the time series.

2. They applied their method on landslides only. In our case, the addition of flash floods to the inventories introduces different types of contrasting GH shapes, slopes and land cover (flash floods tend to be elongated, occur in the valleys with shallower terrain, whereas landslides occurred mainly on the steeper hillslopes) that can influence the SAR time series, specifically if the flash flood enters urbanized area (such as in the DRC GH event) or run through a seasonally dynamic channel with seasonally changing soil moisture levels influencing the SAR signal (Ulaby et al., 1996, Scott et al., 2017).

3. Their used landslide inventories (from Roback et al., 2018 and Emberson et al., 2022) are located in densely vegetated areas (NDVI between 0.6 and 0.8). In agreement with Burrows et al. (2022) our results show that the Uganda GH event, where most of the landscape consists of dense vegetation (i.e. the highest NDVI values), estimated GH event timing accuracies are the highest among all GH events, obtaining a 1-2 images difference from the actual GH event occurrence for SAC (1-16 days) and (detrended) coherence (1-8 days). Although amplitude is overall less performant for the Uganda GH event, we still achieve an accuracy off 13-22 days for the detrended amplitude.

4. We do not threshold on individual GH area. Specifically, the Rwanda GH event contains a GH event size distribution that includes many small individual GH features below the threshold used in Burrows et al. (2022) (fig. 5). Together with the complexity and large fraction of cultivation of the landscape this clearly results in reduced estimation accuracies.

5. They removed landslide timing estimations using the magnitude of change caused by the landslide within the SAR time series, which allowed them to improve the estimation accuracy.

5.3 Improvements and perspectives

The current methodology successfully allows to analyze GH event timing from SAR, but several improvements can be considered in future research.

5.3.1 Improvements

1. In the current methodology we do not detrend individual GH feature time series (see section 3.3). Because detrending does increase timing accuracy within our study, further research on accurate detrending of individual GH time series can potentially greatly benefit timing estimation accuracy.

2. We use one change detection algorithm (ruptures: Truong et al., 2020) to estimate GH event timing. Comparing multiple change detection algorithms (e.g. Deijns et al., 2020, Burrows et al., 2022), could potentially benefit GH event timing estimation accuracy.

3. The quality of the amplitude and coherence imagery is dependent on the quality of the pre-processing applied with the MasTer tool (Derauw et al., 2020, d'Oreye et al., 2021) and how it deals with the different steps such as co-registration, radiometric terrain correction and geocoding. Quality

693 of the imagery in its turn is also dependent on, among others, the multi-look factor (amplitude),
694 the interferometric multi-look factor and the maximum temporal and perpendicular baselines
695 (coherence). In addition, different polarizations may yield different results (Shibayama et al., 2015,
696 Psomiadis, 2016, Park & Lee, 2019) and the use of a different polarization can potentially improve
697 event detectability within the time series. Improvements within the SAR imagery might be achieved
698 by tweaking and closely investigating different pre-processing steps to achieve better image quality.

699 4. The SAC result depends on the ability to find the best reference image (section 3.2). Additional
700 efforts can be made to better find the SAC time series that shows the most significant change
701 related to the GH event occurrence. For example, a preliminary filtering of very noisy SAC time
702 series (before applying our developed method using the ECDF's) can potentially benefit the ability
703 to acquire the best reference image.

704

705 **5.3.2   Perspectives**

706 1. We have studied, for the first time in a GH event timing detection approach, both landslides and
707 flash floods in a combined methodology. Since these GH often co-occur and interact (Marengo &
708 Alves, 2012, Jacobs et al., 2016a, Rengers et al., 2016) they should be analyzed in a multi-hazard
709 approach. Our methodology can be well applied within such an approach. For example, multi-hazard
710 inventories can serve as input for our methodology if there is a need to improve their timing
711 accuracy. Results can subsequently be used in hazard assessment, early warning, and disaster risk
712 reduction strategies.

713 2. Our study shows that there is a clear advantage to analyzing different S1 SAR data products when
714 estimating GH event timing. The fact that Burrows et al. (2022) shows better results for amplitude
715 compared to coherence data is in contrast with our results but reinforces the idea of investigating
716 both data products when applying the methodology to new regions.

717 3. Given the clear influence of landscape and climate as controlling factors for SAR time series behavior
718 (section 2.3), we aimed to develop our methodology within a variety of contrasting landscapes and
719 contrasting vegetation dynamics. This offers perspectives for transferability. We show that slope
720 angle does not seem to influence accuracy (fig. 9). Based on landscape characteristics,
721 transferability to other regions seems therefore likely to acquire good results, specifically for the
722 SAC, coherence and detrended coherence time series as they do seem less influenced by seasonal
723 dynamics than the amplitude and detrended amplitude time series (fig. 6). However, climate drivers
724 could also potentially play a role. For example, since soil moisture and wetness have an influence
725 on amplitude and coherence time series (Ulaby et al., 1996, Srivastava et al., 2006, Brancato et al.,
726 2017, Scott et al., 2017), contrasting precipitation regimes within other regions could potentially
727 influence the response of the SAR time series and the estimated GH event timing accuracy.
728 Examples of contrasting precipitation regimes are: (1) a lower amount of precipitation in more arid
729 regions, or lower/higher amounts in other tropical regions (Fick and Hijmans, 2017); (2) a change
730 in precipitation seasonal variability due to spatially different oscillation of the ITCZ (Nicholson, 2017,
731 Dewitte et al., 2022); (3) the effect of local topography and the presence of lakes on the local

732   precipitation patterns (e.g. Thiery et al., 2015; 2016; 2017, Monsieurs et al., 2018b). The influences
733   of these contrasting precipitation regimes on SAR-based GH timing detection, however, remains to
734   be investigated. Additionally, in its current form, the methodology does not account for the GH
735   events that occur within a time span that is longer than the acquisition time (> 6-12 days) of S1
736   images (i.e. multi-temporal GH events). In that case one would require a time window of
737   occurrence, rather than a specific date. The methodology can be adapted to allow it to derive a
738   time window of GH occurrence. This could mainly be done following the GH event scale, where the
739   start and the end date of the GH event inducing change within the SAR time series (applicable for
740   all data products) should be indicative of the time window of GH event occurrence. However, this
741   remains to be investigated.

742   4. The open-access S1 satellite with its high resolution, high repeat time and global coverage proves
743   to be an excellent data product for estimating GH event timing and allows for our developed
744   methodology to be applied on every region of the world. The use of our methodology with different
745   satellite products (e.g. COSMO-SkyMed, upcoming NISAR satellite) is not straightforward. Different
746   available SAR satellite products operate in different bands with their own characteristics (e.g. X-
747   band for COSMO-SkyMed (Covello et al., 2010) and L-band for NISAR (NISAR, 2018)), that will likely
748   have implications on the ability for accurate GH event timing estimation. For example, the varying
749   vegetation penetration depths associated with different SAR bands (Dzurisin, 2006) will likely have
750   an influence on the impact of seasonal vegetation dynamics on the SAR time series as observed for
751   our GH events (fig. 6).

752   5. The methodology can benefit (in terms of data availability, scalability, and processing time) from
753   implementation on a cloud computing service. Cloud computing platforms such as GEE only provide
754   pre-processed amplitude imagery (i.e. amplitude ground range detected imagery). As such, they
755   allow for the applicability of our methodology using the amplitude, detrended amplitude and SAC
756   data products. To our knowledge, so far, no cloud computing platform offer the possibility for
757   processing and using coherence data. Additionally, the use of pre-processed amplitude imagery
758   restrains us from manual input during the pre-processing step (as the MasTer Toolbox allows).

759   6. The methodology can potentially be combined with optical data (e.g. Deijns et al., 2020) that could
760   serve as additional data to help narrow down the time window and filter out any non-sense timing
761   estimations.

6. Conclusion

763   We established a regionally applicable methodology to automatically determine GH event timing from
764   SAR images, that can be applied without prior knowledge of the GH event. We successfully assessed
765   the use of multiple SAR derived data products in their ability to accurately detect GH event timing in
766   contrasting landscapes. We show that landslides and flash floods can be detected and studied together,
767   hence we open new perspectives in the study of multi-hazards, that can subsequently aid in hazard
768   assessment, early warning, and disaster risk reduction strategies. Our methodology has the potential to

be combined with existing spatial detection methods to support inventory creation and boost GH event research in remote inaccessible areas such as the African cloud-covered tropics.

From a data processing point of view, the methodology is established around an unprecedented analysis of various SAR products coming from Sentinel-1 (S1) images. We show that there is a need to investigate different SAR data products when estimating GH event timing (amplitude, spatial amplitude correlation, and coherence) since the signal response can be different and sometimes contradictory when looking at one single event. The implementation of our methodology on a cloud computing platform can be beneficial in terms of scalability, data availability and processing time. However, the main limitations in this context are: (1) no control in pre-processing of S1 imagery and, (2) S1 coherence data is so far not available within these platforms.

With a focus on four events containing a total of about 2500 landslides and flash flood features in contrasting landscapes, we propose a methodology that is adapted to be applied to other regions. Here, we focused on tropical environments where climate conditions and land use dynamics are rather specific. However, we believe that the complexity of these landscapes is an added value for the transferability of the methodology. Additionally, the use of the globally available open access S1 satellite data allows our methodology to be applied on every region of the World.

Acknowledgement

This study was supported by the Belgium Science Policy (BELSPO) through the PAStECA project (BR/165/A3/PASTECA) entitled "Historical Aerial Photographs and Archives to Assess Environmental Changes in Central Africa" (http://pasteca.africamuseum.be), and the GEOTROP project (B2/223/P1/GEOTROP) entitled "Geomorphic hazards and compound events in a changing tropical East Africa". The compilation of the inventory data benefited from field-based insight and discussion with Arthur Depicker, Josué Mugisho Bachinyaga, John Sekajugo and Judith Uwihirwe. PlanetScope data provided by the European Space Agency.

Code and data availability

Sentinel-1 and Sentinel-2 data are provided open-access by the European Space Agency. Landsat 8 data are provided open access by the U.S. Geological Survey. The Python scripts for the GH event timing estimation, sensitivity analysis, and precipitation analysis and the Google Earth Engine code for vegetation analysis can be accessed at: https://doi.org/10.5281/zenodo.7198346. The four GH inventories can be downloaded at: https://doi.org/10.5281/zenodo.7198322

Author contribution

AAJD, OD, FK and WT conceived the study. AAJD compiled the landslide and flash flood inventory with the support of OD. AAJD processed and analyzed the data. OD conducted field work for the validation of the inventory. AAJD wrote the original draft of the manuscript, with key initial input from OD and FK. NO trained AAJD in SAR image pre-processing. All the authors contributed to reviewing and editing the manuscript. OD obtained funding for this work.

Competing interests.

The authors declare no conflict of interest.

References

Aimaiti, Y., Liu, W., Yamazaki, F. and Maruyama, Y.: Earthquake-induced landslide mapping for the 2018 Hokkaido Eastern Iburi earthquake using PALSAR-2 data. Remote Sens., 11i, 2351, https://doi.org/10.3390/rs11202351, 2019

Ali, K., Bajracharyar, R.M. and Raut, N.: Advances and challenges in flash flood risk assessment: A review. J. Geogr. Nat. Disast. 2017, 7, 1-6, https://doi.org/10.4172/2167-0587.1000195, 2017

Bai, J.: Estimating multiple breaks one at a time. Econ. Theory, 13, 315-352, https://doi.org/10.1017/S0266466600005831, 1997

Balzter, H.: Forest mapping and monitoring with interferometric synthetic aperture radar (InSAR). Prog. Phys. Geogr., 25, 159-177, https://doi.org/10.1177/030913330102500201, 2001

Bamler, R.: Principles of synthetic aperture radar. Surv. Geophys., 21, 147-157, https://doi.org/10.1023/A:1006790026612, 2000

Barrett, B., Whelan, P. and Dwyer, E.: The use of C-and L-band repeat-pass interferometric SAR coherence for soil moisture change detection in vegetated areas. Open Remote Sens. J., 5, 37-53, https://doi.org/10.2174/1875413901205010037, 2012

Behling, R., Roessner, S., Kaufmann, H. and Kleinschmit, B.: Automated spatiotemporal landslide mapping over large areas using rapideye time series data. Remote Sens., 6, 8026-8055. https://doi.org/10.3390/rs6098026, 2014

825 Behling, R., Roessner, S., Golovko, D. and Kleinschmit, B.: Derivation of long-term spatiotemporal
826 landslide activity—A multi-sensor time series approach. Remote Sens. Environ., 186, 88-104,
827 https://doi.org/10.1016/j.rse.2016.07.017, 2016

828 Bonfils, S.: Trend analysis of the mean annual temperature in Rwanda during the last fifty two years. J.
829 Environ. Prot. 3, 20077, https://doi.org/10.4236/jep.2012.36065, 2012.

830 Bradshaw, C.J. A., Sodhi, N.S., Peh, K.S.H., Brook, B.W.: Global evidence that deforestation amplifies
831 flood risk and severity in the developing world. Glob. Chang. Biol. 13, 2379–2395,
832 https://doi.org/10.1111/j.1365-2486.2007.01446.x, 2007

833 Brancato, V., Liebisch, F. and Hajnsek, I.: Impact of plant surface moisture on differential interferometric
834 observables: A controlled electromagnetic experiment. IEEE Trans. Geosci. Remote Sens., 55, 3949-
835 3964, https://doi.org/10.1109/TGRS.2017.2684814, 2017

836 Burrows, K., Walters, R.J., Milledge, D., Spaans, K. and Densmore, A.L.: A new method for large-scale
837 landslide classification from satellite radar. Remote Sens., 11, 237, https://doi.org/10.3390/rs11030237,
838 2019

839 Burrows, K., Walters, R. J., Milledge, D., and Densmore, A. L.: A systematic exploration of satellite radar
840 coherence methods for rapid landslide detection, Nat. Hazards Earth Syst. Sci., 20, 3197–3214,
841 https://doi.org/10.5194/nhess-20-3197-2020, 2020.

842 Burrows, K., Marc, O., and Remy, D.: Using Sentinel-1 radar amplitude time series to constrain the
843 timings of individual landslides: a step towards understanding the controls on monsoon-triggered
844 landsliding, Nat. Hazards Earth Syst. Sci., 22, 2637–2653, https://doi.org/10.5194/nhess-22-2637-2022,
845 2022

846 Casagli, N., Frodella, W., Morelli, S., Tofani, V., Ciampalini, A., Intrieri, E., Raspini, F., Rossi, G., Tanteri,
847 L., Lu, P.: Spaceborne, UAV and ground-based remote sensing techniques for landslide mapping,
848 monitoring and early warning. Geoenviron. Disasters 4, 9. https://doi.org/10.1186/s40677-017-0073-
849 1, 2017

850 Chen, X.L., Liu, C.G., Chang, Z.F. and Zhou, Q.: The relationship between the slope angle and the
851 landslide size derived from limit equilibrium simulations. Geomorphology, 253, 547-550,
852 https://doi.org/10.1016/j.geomorph.2015.01.036, 2016

853 Colesanti, C. and Wasowski, J.: Investigating landslides with space-borne Synthetic Aperture Radar
854 (SAR) interferometry. Eng. Geol., 88, 173-199, https://doi.org/10.1016/j.enggeo.2006.09.013, 2006

855 Covello, F., Battazza, F., Coletta, A., Lopinto, E., Fiorentino, C., Pietranera, L., Valentini, G. and Zoffoli,
856 S.: COSMO-SkyMed an existing opportunity for observing the Earth. J. Geodyn. 49, 171-180,
857 https://doi.org/10.1016/j.jog.2010.01.001, 2010

858 Deijns, A.A.J., Bevington, A.R., van Zadelhoff, F., de Jong, S.M., Geertsema, M. and McDougall, S.:
859 Semi-automated detection of landslide timing using harmonic modelling of satellite imagery,
860 Buckinghorse River, Canada. Int. J. Appl. Earth Obs. Geoinf, 84, 101943,
861 https://doi.org/10.1016/j.jag.2019.101943, 2020

862 Depicker, A., Jacobs, L., Mboga, N., Smets, B., Van Rompaey, A., Lennert, M., Wolff, E., Kervyn, F.,
863 Michellier, C., Dewitte, O. and Govers, G.: Historical dynamics of landslide risk from population and
864 forest-cover changes in the Kivu Rift. Nat. Sustain., 4, 965-974, https://doi.org/10.1038/s41893-021-
865 00757-9, 2021

866 Derauw, D., Libert, L., Barbier, C., Orban, A., Kervyn, F., Samsonov, S., d'Oreye, N.: The CSL InSAR
867 Suite processor: specificities of a command line InSAR processing software specifically adapted for
868 automated time series processing. ESA Living Planet Symposium 2019, Milano, Italy, 2019. Abstract,
869 13–17., 2019

870 Derauw, D., Jaspard, M., Caselli, A. and Samsonov, S.: Ongoing automated ground deformation
871 monitoring of Domuyo-Laguna del Maule area (Argentina) using Sentinel-1 MSBAS time series:
872 Methodology description and first observations for the period 2015–2020, J. S. Am. Earth Sci., 104,
873 102850, https://doi.org/10.1016/j.jsames.2020.102850, 2020

874 DeVries, B., Huang, C., Armston, J., Huang, W., Jones, J.W. and Lang, M.W.: Rapid and robust
875 monitoring of flood events using Sentinel-1 and Landsat data on the Google Earth Engine. Remote Sens.
876 Environ., 240, 111664, https://doi.org/10.1016/j.rse.2020.111664, 2020

877 Dewitte, O., Dille, A., Depicker, A., Kubwimana, D., Maki Mateso, J.-C., Mugaruka Bibentyo, T.,
878 Uwihirwe, J. and Monsieurs, E.: Constraining landslide timing in a data-scarce context: from recent to
879 very old processes in the tropical environment of the North Tanganyika-Kivu Rift region. Landslides, 18,
880 161-177, https://doi.org/10.1007/s10346-020-01452-0, 2021

881 Dewitte, O., Depicker, A., Moeyersons, J. and Dille, A.: Mass Movements in Tropical Climates.: Treatise
882 on Geomorphology, vol. 5, Shroder, J.J.F. (Ed.), Elsevier, Academic Press, 338–349,
883 https://doi.org/10.1016/B978-0-12-818234-5.00118-8, 2022

884 Dobson, M.C. and Ulaby, F.T.: Active microwave soil moisture research. IEEE Trans. Geosci. Remote
885 Sens., 1, 23-36, https://doi.org/10.1109/TGRS.1986.289585, 1986

886 Dubois, P.C., Van Zyl, J. and Engman, T.: Measuring soil moisture with imaging radars. IEEE Trans.
887 Geosci. Remote Sens., 33, 915-926, https://doi.org/10.1109/36.406677, 1995

888 Dzurisin, D.: Volcano deformation: new geodetic monitoring techniques. Springer,
889 https://doi.org/10.1007/978-3-540-49302-0, 2006

890 Emberson, R., Kirschbaum, D. and Stanley, T.: New global characterisation of landslide exposure. Nat.
891 Hazards Earth Syst. Sci., 20, 3413-3424. https://doi.org/10.5194/nhess-20-3413-2020, 2020

892 Emberson, R., Kirschbaum, D. B., Amatya, P., Tanyas, H., and Marc, O.: Insights from the topographic
893 characteristics of a large global catalog of rainfall-induced landslide event inventories, Nat. Hazards
894 Earth Syst. Sci., 22, 1129–1149, https://doi.org/10.5194/nhess-22-1129-2022, 2022.

895 ESA Climate Change Initiative–Land Cover Project 2017. 20 m Resolution, European Space Agency,
896 2016.

897 Esposito, G., Marchesini, I., Mondini, A. C., Reichenbach, P., Rossi, M., and Sterlacchini, S.: A
898 spaceborne SAR-based procedure to support the detection of landslides, Nat. Hazards Earth Syst. Sci.,
899 20, 2379–2395, https://doi.org/10.5194/nhess-20-2379-2020, 2020.

900 Fick, S.E. and Hijmans, R.J.: WorldClim 2: new 1-km spatial resolution climate surfaces for global land
901 areas. Int. J. Climatol., 37, 4302-4315, https://doi.org/10.1002/joc.5086, 2017

902 Foga, S., Scaramuzza, P.L., Guo, S., Zhu, Z., Dilley Jr, R.D., Beckmann, T., Schmidt, G.L., Dwyer, J.L.,
903 Hughes, M.J. and Laue, B.: Cloud detection algorithm comparison and validation for operational Landsat
904 data products. Remote Sens. Environ., 194, 379-390, https://doi.org/10.1016/j.rse.2017.03.026, 2017

905 Foody, G.M. and Mathur, A.: The use of small training sets containing mixed pixels for accurate hard
906 image classification: Training on mixed spectral responses for classification by a SVM. Remote Sens.
907 Environ., 103, 179-189, https://doi.org/10.1016/j.rse.2006.04.001, 2006

908 Froude, M. J. and Petley, D. N.: Global fatal landslide occurrence from 2004 to 2016, Nat. Hazards Earth
909 Syst. Sci., 18, 2161–2181, https://doi.org/10.5194/nhess-18-2161-2018, 2018.

910 Fryzlewicz, P.: Wild binary segmentation for multiple change-point detection. Ann. Stat., 42, 2243-2281,
911 https://doi.org/10.1214/14-AOS1245, 2014

912 Ge, P., Gokon, H., Meguro, K. and Koshimura, S.: Study on the intensity and coherence information of
913 high-resolution ALOS-2 SAR images for rapid massive landslide mapping at a pixel level. Remote Sens.,
914 11, 2808, https://doi.org/10.3390/rs11232808, 2019

915 Giertz, S., Junge, B. and Diekkrüger, B.: Assessing the effects of land use change on soil physical
916 properties and hydrological processes in the sub-humid tropical environment of West Africa. Phys.
917 Chem. Earth, 30, 485-496, https://doi.org/10.1016/j.pce.2005.07.003, 2005

918 Gorelick, N., Hancher, M., Dixon, M., Ilyushchenko, S., Thau, D. and Moore, R.: Google Earth Engine:
919 Planetary-scale geospatial analysis for everyone. Remote Sens. Environ., 202, 18-27,
920 https://doi.org/10.1016/j.rse.2017.06.031, 2017

921 Guzzetti, F., Peruccacci, S., Rossi, M. and Stark, C.P.: he rainfall intensity–duration control of shallow
922 landslides and debris flows: an update. Landslides 5, 3–17, https://doi.org/10.1007/s10346-007-0112-
923 1, 2008

924 Guzzetti, F., Mondini, A.C., Cardinali, M., Fiorucci, F., Santangelo, M., Chang, K.-T.: Landslide inventory
925 maps: New tools for an old problem. Earth-Sci. Rev., 112, 42–66,
926 https://doi.org/10.1016/j.earscirev.2012.02.001, 2012

927 Guzzetti, F., Gariano, S.L., Peruccacci, S., Brunetti, M.T., Marchesini, I., Rossi, M. and Melillo, M.:
928 Geographical landslide early warning systems. Earth-Science Reviews, 200, 102973,
929 https://doi.org/10.1016/j.earscirev.2019.102973, 2020

930 Hagberg, J.O., Ulander, L.M. and Askne, J.: Repeat-pass SAR interferometry over forested terrain. IEEE
931 Trans. Geosci. Remote Sens., 33, 331-340, https://doi.org/10.1109/TGRS.1995.8746014, 1995

932 Handwerger, A. L., Huang, M.-H., Jones, S. Y., Amatya, P., Kerner, H. R., and Kirschbaum, D. B.:
933 Generating landslide density heatmaps for rapid detection using open-access satellite radar data in
934 Google Earth Engine, Nat. Hazards Earth Syst. Sci., 22, 753–773, https://doi.org/10.5194/nhess-22-
935 753-2022, 2022.

936 Hanssen, R.F.: Radar interferometry: data interpretation and error analysis, vol 2, Springer,
937 https://doi.org/10.1007/0-306-47633-9, 2001

938 Heri-Kazi, A. B. and Bielders, C. L.: Cropland characteristics and extent of soil loss by rill and gully
939 erosion in smallholder farms in the KIVU highlands, D.R. Congo, Geoderma Reg., 26, e00404,
940 https://doi.org/10.1016/j.geodrs.2021.e00404, 2021.

941 Intrieri, E., Raspini, F., Fumagalli, A., Lu, P., Del Conte, S., Farina, P., Allievi, J., Ferretti, A. and Casagli,
942 N.: The Maoxian landslide as seen from space: detecting precursors of failure with Sentinel-1 data.
943 Landslides, 15, 123-133, https://doi.org/10.1007/s10346-017-0915-7, 2018

944 Jacobs, L., Maes, J., Mertens, K., Sekajugo, J., Thiery, W., Van Lipzig, N., Poesen, J., Kervyn, M.,
945 Dewitte, O.: Reconstruction of a flash flood event through a multi-hazard approach: focus on the
946 Rwenzori Mountains, Uganda. Nat. Hazards 84, 851–876, https://doi.org/10.1007/s11069-016-2458-y,
947 2016a.

948 Jacobs, L., Dewitte, O., Poesen, J., Delvaux, D., Thiery, W. and Kervyn, M.: The Rwenzori Mountains, a
949 landslide-prone region?, Landslides, 13, 519-536. https://doi.org/10.1007/s10346-015-0582-5, 2016b

950 Jacobs, L., Kabaseke, C., Bwambale, B., Katutu, R., Dewitte, O., Mertens, K., Maes, J. and Kervyn, M.:
951 The geo-observer network: A proof of concept on participatory sensing of disasters in a remote setting.
952 Sci. Total Environ., 670, 245-261, https://doi.org/10.1016/j.scitotenv.2019.03.177, 2019

953 Jacquemart, M. and Tiampo, K.: Leveraging time series analysis of radar coherence and normalized
954 difference vegetation index ratios to characterize pre-failure activity of the Mud Creek landslide,
955 California, Nat. Hazards Earth Syst. Sci., 21, 629–642, https://doi.org/10.5194/nhess-21-629-2021,
956 2021.

957 Joyce, K.E., Belliss, S.E., Samsonov, S.V., McNeill, S.J. and Glassey, P.J.: A review of the status of
958 satellite remote sensing and image processing techniques for mapping natural hazards and disasters.
959 Prog. Phys. Geogr., 33, 183-207, https://doi.org/10.1177/0309133309339563, 2009

960 Jung, J. and Yun, S.H.: Evaluation of coherent and incoherent landslide detection methods based on
961 Synthetic Aperture Radar for rapid response: A case study for the 2018 Hokkaido landslides. Remote
962 Sens., 12, 265, https://doi.org/10.3390/rs12020265, 2020

963 Kennedy, R.E., Yang, Z., Gorelick, N., Braaten, J., Cavalcante, L., Cohen, W.B., Healey, S.:
964 Implementation of the LandTrendr algorithm on google earth engine. Remote Sens. 10, 691.
965 https://doi.org/10.3390/rs10050691. 2018

966 Kjekstad, O., Highland, L.: Economic and Social Impacts of Landslides. Landslides – Disaster Risk
967 Reduction. Sassa, K., Canuti, P. (eds), Springer, Berlin, Heidelberg. https://doi.org/10.1007/978-3-540-
968 69970-5_30, 2009

969 Komac M, Holley R, Mahapatra P, van der Marel H, Bavec M.: Coupling of GPS/GNSS and radar
970 interferometric data for a 3D surface displacement monitoring of landslides. Landslides 12, 241–257,
971 https://doi.org/10.1007/s10346-014-0482-0, 2015

972 Konishi, T. and Suga, Y.: Landslide detection using COSMO-SkyMed images: A case study of a landslide
973 event on Kii Peninsula, Japan. Eur. J. Remote Sens, 51, 205-221,
974 https://doi.org/10.1080/22797254.2017.1418185, 2018

975 Korup, O., Densmore, A.L. and Schlunegger, F.: The role of landslides in mountain range evolution.
976 Geomorphology, 120, 77-90, https://doi.org/10.1016/j.geomorph.2009.09.017, 2010

977 Kubwimana, D., Ait Brahim, L., Nkurunziza, P., Dille, A., Depicker, A., Nahimana, L., Abdelouafi, A. and
978 Dewitte, O.: Characteristics and Distribution of Landslides in the Populated Hillslopes of Bujumbura,
979 Burundi. Geosci., 11, 259, https://doi.org/10.3390/geosciences11060259, 2021

980 Le Cozannet, G., Kervyn, M., Russo, S., Ifejika Speranza, C., Ferrier, P., Foumelis, M., Lopez, T.,
981 Modaressi, H.: Space-Based Earth Observations for Disaster Risk Management. Surv. Geophys. 41,
982 1209–1235, https://doi.org/10.1007/s10712-020-09586-5, 2020

983 Liu, C., Guo, L., Ye, L., Zhang, S., Zhao, Y. and Song, T.: A review of advances in China's flash flood
984 early-warning system. Nat. Hazards 92, 619–634. https://doi.org/10.1007/s11069-018-3173-7, 2018

985 Marc, O., Stumpf, A., Malet, J.-P., Gosset, M., Uchida, T., and Chiang, S.-H.: Initial insights from a global
986 database of rainfall-induced landslide inventories: the weak influence of slope and strong influence of
987 total storm rainfall, Earth Surf. Dynam., 6, 903–922, https://doi.org/10.5194/esurf-6-903-2018, 2018.

988 Marengo, J.A. and Alves, L.M.: The 2011 intense rainfall and floods in Rio De Janeiro, Bulletin of the
989 American Meteorological Society, 93, 1-282, 2012

990 Martinis, S., Kuenzer, C., Wendleder, A., Huth, J., Twele, A., Roth, A. and Dech, S.: Comparing four
991 operational SAR-based water and flood detection approaches. Int. J. Remote Sens., 36, 3519-3543,
992 https://doi.org/10.1080/01431161.2015.1060647, 2015

993 Mohan, A., Singh, A.K., Kumar, B. and Dwivedi, R.: Review on remote sensing methods for landslide
994 detection using machine and deep learning. Trans. Emerg. Telecommun. Technol. T, 32, 3998.
995 https://doi.org/10.1002/ett.3998, 2021

996 Mondini, A.C.: Measures of spatial autocorrelation changes in multitemporal SAR images for event
997 landslides detection. Remote Sens., 9, 554, https://doi.org/10.3390/rs9060554, 2017

998 Mondini, A.C., Santangelo, M., Rocchetti, M., Rossetto, E., Manconi, A. and Monserrat, O.: Sentinel-1
999 SAR amplitude imagery for rapid landslide detection. Remote Sens., 11, 760,
1000 https://doi.org/10.3390/rs11070760, 2019

1001 Mondini, A.C., Guzzetti, F., Chang, K.T., Monserrat, O., Martha, T.R. and Manconi, A.: Landslide failures
1002 detection and mapping using Synthetic Aperture Radar: Past, present and future. Earth-Sci. Rev., 216,
1003 103574, https://doi.org/10.1016/j.earscirev.2021.103574, 2021

1004 Monsieurs, E., Jacobs, L., Michellier, C., Basimike Tchangaboba, J., Bamulezi Ganza, G., Kervyn, F.,
1005 Maki Mateso, J.-C., Mugaruka Bibentyo, T., Kalikone Buzera, C., Nahimana, L. Ndayisenga, A.,
1006 Nkurunziza, P., Thiery, W., Demoulin, A., Kervyn M. and Dewitte, O.: Landslide inventory for hazard
1007 assessment in a data-poor context: a regional-scale approach in a tropical African environment.
1008 Landslides, 15, 2195-2209, https://doi.org/10.1007/s10346-018-1008-y, 2018a

1009 Monsieurs, E., Kirschbaum, D.B., Tan, J., Maki Mateso, J.-C., Jacobs, L., Plisnier, P.-D., Thiery, W.,
1010 Umutoni, A., Musoni, D., Mugaruka Bibentyo, T. Bamulezi Ganza, G., Ilombe Mawe, G., Bagalwa, L.,
1011 Kankurize, C., Michellier, C., Stanley, T., Kervyn, F., Kervyn, M., Demoulin, A., and Dewitte, O.:
1012 Evaluating TMPA rainfall over the sparsely gauged East African Rift. J. Hydrometeorol., 19, 1507-1528,
1013 https://doi.org/10.1175/JHM-D-18-0103.1, 2018b

1014 Monsieurs, E., Dewitte, O., and Demoulin, A.: A susceptibility-based rainfall threshold approach for
1015 landslide occurrence, Nat. Hazards Earth Syst. Sci., 19, 775–789, https://doi.org/10.5194/nhess-19-
1016 775-2019, 2019.

1017 Monsieurs, E.: The potential of satellite rainfall estimates in assessing regional landslide hazard in
1018 Central Africa (Doctoral dissertation, Université de Liège, Liège, Belgium),
1019 https://hdl.handle.net/2268/245576, 2020

1020 Nakulopa, F., Vanderkelen, I., Van de Walle, J., Van Lipzig, N.P., Tabari, H., Jacobs, L., Tweheyo, C.,
1021 Dewitte, O. and Thiery, W.: Evaluation of high-resolution precipitation products over the Rwenzori
1022 Mountains (Uganda). J. Hydrometeorol., 23, 747-768, https://doi.org/10.1175/JHM-D-21-0106.1, 2022

1023 Nicholson, S. E.: Climate and climatic variability of rainfall over eastern Africa, Rev. Geophys., 5, 590–
1024 635, https://doi.org/10.1002/2016RG000544, 2017

1025 NISAR, NASA-ISRO SAR (NISAR) Mission Science Users' Handbook. NASA Jet Propulsion Laboratory,
1026 261, 18-1893., 2018

1027 Nobile, A., Dille, A., Monsieurs, E., Basimike, J., Mugaruka Bibentyo, T., d'Oreye, N., Kervyn, F. and
1028 Dewitte, O. Multi-temporal DInSAR to characterise landslide ground deformations in a tropical urban
1029 environment: Focus   on   Bukavu   (DR   Congo).   Remote   Sens.,   10,   626,
1030 https://doi.org/10.3390/rs10040626, 2018

1031 Nolan, M. and Fatland, D.R.: Penetration depth as a DInSAR observable and proxy for soil moisture.
1032 IEEE Trans. Geosci. Remote Sens., 41, 532-537, https://doi.org/10.1109/TGRS.2003.809931, 2003

1033 d'Oreye, N., Derauw, D., Libert, L., Samsonov, S., Dille, A., Nobile, A., Monsieurs, E., Dewitte, O.,
1034 Kervyn, F.: Automatization of InSAR mass processing using CSL InSAR Suite (CIS) software for
1035 Multidimensional Small Baseline Subset (MSBAS) analysis: example combining Sentinel-1 and Cosmo-
1036 SkyMed SAR data for landslides monitoring in South Kivu, DR Congo. ESA Living Planet Symposium
1037 2019, Milano, Italy, 2019

1038 d'Oreye, N., Derauw, D., Samsonov, S., Jaspard, M. and Smittarello, D.: MasTer: A Full Automatic Multi-
1039 Satellite InSAR Mass Processing Tool for Rapid Incremental 2D Ground Deformation Time Series. Int.
1040 Geosci.   Remote   Sens.   Symp.   (IGARSS),   1899-1902,
1041 https://doi.org/10.1109/IGARSS47720.2021.9553615, 2021

1042 Park, S.E. and Lee, S.G.: On the use of single-, dual-, and quad-polarimetric SAR observation for
1043 landslide detection. ISPRS Int. J. Geo-Inf., 8, 384, https://doi.org/10.3390/ijgi8090384, 2019

1044 Petersen, M.S.: Impacts of Flash Floods. Coping With Flash Floods. NATO Science Series, vol 77,
1045 Gruntfest, E., Handmer, J. (eds), Springer, Dordrecht. https://doi.org/10.1007/978-94-010-0918-8_2,
1046 2001

1047 Peterson, M., Mach, D., Buechler, D.: A Global LIS/OTD Climatology of Lightning Flash Extent Density.
1048 J. Geophys. Res. Atmos. 126. https://doi.org/10.1029/2020JD033885, 2021

1049 Planet Team. Planet Application Program Interface: In Space for Life on Earth. San Francisco, CA.
1050 https://api.planet.com, 2017

1051 Psomiadis, E.: October. Flash flood area mapping utilising SENTINEL-1 radar data, Earth Resour.
1052 Environ. Remote Sens./GIS App. VII, 10005, 100051G, https://doi.org/10.1117/12.2241055, 2016

1053 Rengers, F.K., McGuire, L.A., Kean, J.W., Staley, D.M., Hobley, D.E.J.: Model simulations of flood and
1054 debris flow timing in steep catchments after wildfire. Water Resour. Res. 52, 6041–6061,
1055 https://doi.org/10.1002/2015WR018176, 2016.

1056 Roback, K., Clark, M.K., West, A.J., Zekkos, D., Li, G., Gallen, S.F., Chamlagain, D. and Godt, J.W.: The
1057 size, distribution, and mobility of landslides caused by the 2015 Mw7. 8 Gorkha earthquake, Nepal.
1058 Geomorphology, 301, 121-138, https://doi.org/10.1016/j.geomorph.2017.01.030, 2018

1059 Robinson, T.R., Rosser, N., Walters, R.J.: The Spatial and Temporal Influence of Cloud Cover on
1060 Satellite-Based Emergency Mapping of Earthquake Disasters. Sci. Rep. 9, 1–9.
1061 https://doi.org/10.1038/s41598-019-49008-0, 2019

1062 Rocca, F., Prati, C., Monti Guarnieri, A., Ferretti, A.: SAR interferometry and its applications. Surv.
1063 Geophys. 21, 159–176. https://doi.org/10.1023/A:1006710731155, 2000

1064 Samsonov, S., d'Oreye, N.: Multidimensional time-series analysis of ground deformation from multiple
1065 InSAR data sets applied to Virunga Volcanic Province. Geophys. J. Int. 191, 1095–1108.
1066 https://doi.org/10.1111/j.1365-246X.2012.05669.x, 2012

1067 Scott, C.P., Lohman, R.B. and Jordan, T.E.: InSAR constraints on soil moisture evolution after the March
1068 2015 extreme precipitation event in Chile. Sci. Rep., 7, 1-9. https://doi.org/10.1038/s41598-017-05123-
1069 4, 2017

1070 Sekajugo, J., Kagoro-Rugunda, G., Mutyebere, R., Kabaseke, C., Namara, E., Dewitte, O., Kervyn, M.,
1071 and Jacobs, L.: Can citizen scientists provide a reliable geo-hydrological hazard inventory? An analysis
1072 of biases, sensitivity and precision for the Rwenzori Mountains, Uganda, Environ. Res. Lett., 17, 045011,
1073 https://doi.org/10.1088/1748-9326/ac5bb5, 2022.

1074 Shibayama, T., Yamaguchi, Y. and Yamada, H.: Polarimetric scattering properties of landslides in
1075 forested areas and the dependence on the local incidence angle. Remote Sens., 7, 15424-15442,
1076 https://doi.org/10.3390/rs71115424, 2015

1077 Small, D.: Flattening gamma: Radiometric terrain correction for SAR imagery. IEEE Trans. Geosci.
1078 Remote Sens., 49, 3081-3093, https://doi.org/10.1109/TGRS.2011.2120616, 2011

1079 Solari, L., Del Soldato, M., Raspini, F., Barra, A., Bianchini, S., Confuorto, P., Casagli, N. and Crosetto,
1080 M. Review of satellite interferometry for landslide detection in Italy. Rem. Sens., 12, 1351.
1081 https://doi.org/10.3390/rs12081351, 2020

1082 Srivastava, H.S., Patel, P. and Navalgund, R.R.: How far SAR has fulfilled its expectation for soil moisture
1083 retrieval. Microwave. Remote Sens. Atm. Env. 6410, 641001 https://doi.org/10.1117/12.693946, 2006

1084 Strozzi, T., Dammert, P.B., Wegmuller, U., Martinez, J.M., Askne, J.I., Beaudoin, A. and Hallikainen,
1085 N.T.: Landuse mapping with ERS SAR interferometry. IEEE Trans. Geosci. Remote Sens., 38, 766-775,
1086 https://doi.org/10.1109/36.842005, 2000

1087   Stumpf, A., Malet, J.P., Allemand, P. and Ulrich, P.: Surface reconstruction and landslide displacement
1088   measurements with Pléiades satellite images. ISPRS J. Photogramm. Remote Sens., 95, 1-12,
1089   https://doi.org/10.1016/j.isprsjprs.2014.05.008, 2014

1090   Tessari, G., Floris, M. and Pasquali, P.: Phase and amplitude analyses of SAR data for landslide detection
1091   and monitoring in non-urban areas located in the North-Eastern Italian pre-Alps. Environmental Earth
1092   Sciences, 76, 85, https://doi.org/10.1007/s12665-017-6403-5, 2017

1093   Thiery, W., Davin, E.L., Panitz, H.-J., Demuzere, M., Lhermitte, S., van Lipzig, N.P.M.: The impact of
1094   the African Great Lakes on the regional climate, J. Climate, 28, 4061-4085,
1095   https://doi.org/10.1175/JCLI-D-14-00565.1, 2015.

1096   Thiery, W., Davin, E.L., Seneviratne, S.I., Bedka, K., Lhermitte, S., van Lipzig, N.P.M.: Hazardous
1097   thunderstorm   intensification   over   Lake   Victoria,   Nat.   Comm.,   7,   12786,
1098   https://doi.org/10.1038/ncomms12786, 2016

1099   Thiery, W., Gudmundsson, L., Bedka, K., Semazzi, F.H.M., Lhermitte, S., Willems, P., van Lipzig, N.P.M.,
1100   Seneviratne, S.I.: Early warnings of hazardous thunderstorms over Lake Victoria, Env. Res. Lett., 12,
1101   074012, https://doi.org/10.1088/1748-9326/aa7521, 2017

1102   Truong, C., Oudre, L. and Vayatis, N.: Selective review of offline change point detection methods. Signal
1103   Process., 167, 107299, https://doi.org/10.1016/j.sigpro.2019.107299, 2020

1104   Tucker, C.J.: Red and photographic infrared linear combinations for monitoring vegetation. Remote
1105   Sens. Environ. 8, 127–150. https://doi.org/10.1016/0034- 4257(79)90013-0, 1979

1106   Turkington, T., Ettema, J., van Westen, C. J., and Breinl, K.: Empirical atmospheric thresholds for debris
1107   flows and flash floods in the southern French Alps, Nat. Hazards Earth Syst. Sci., 14, 1517–1530,
1108   https://doi.org/10.5194/nhess-14-1517-2014, 2014.

1109   Twele, A., Cao, W., Plank, S. and Martinis, S.: Sentinel-1-based flood mapping: a fully automated
1110   processing   chain.   Int.   J.   Remote   Sens.,   37,   2990-3004,
1111   https://doi.org/10.1080/01431161.2016.1192304, 2016

1112   Tzouvaras, M., Danezis, C. and Hadjimitsis, D.G.: Small scale landslide detection using Sentinel-1
1113   interferometric SAR coherence. Remote Sens., 12, 1560, https://doi.org/10.3390/rs12101560, 2020

1114   Ulaby, F.T., Dubois, P.C. and Van Zyl, J.: Radar mapping of surface soil moisture. J. Hydrol., 184, 57-
1115   84, https://doi.org/10.1016/0022-1694(95)02968-0, 1996

1116   Van de Walle, J., Thiery, W., Brousse, O., Souverijns, N., Demuzere, M., and van Lipzig, N.P.M.: A
1117   convection-permitting model for the Lake Victoria Basin: Evaluation and insight into the mesoscale
1118   versus synoptic atmospheric dynamics. Clim. Dyn., 54, 1779-1799. https://doi.org/10.1007/s00382-
1119   019-05088-2, 2020

1120 van Westen, C.J., Castellanos, E., Kuriakose, S.L.: Spatial data for landslide susceptibility, hazard, and
1121 vulnerability assessment: An overview. Eng. Geol. 2008, 102, 112–131,
1122 https://doi.org/10.1016/j.enggeo.2008.03.010, 2008

1123 Weydahl, D.J.: Analysis of ERS SAR coherence images acquired over vegetated areas and urban
1124 features. Int. J. Remote Sens., 22, 2811-2830, https://doi.org/10.1080/01431160010006412, 2001

1125 Zebker, H.A. and Villasenor, J.: Decorrelation in interferometric radar echoes. IEEE Trans. Geosci.
1126 Remote Sens., 30, 950-959, https://doi.org/10.1109/36.175330, 1992

1127 Zhong, C., Li, C., Gao, P. and Li, H.: Discovering Vegetation Recovery and Landslide Activities in the
1128 Wenchuan Earthquake Area with Landsat Imagery. Sensors, 21, 5243,
1129 https://doi.org/10.3390/s21155243, 2021